UNIVERSIDADE DE LISBOA
FACULDADE DE CIÊNCIAS
DEPARTAMENTO DE FÍSICA


# The design and manufacture of an anthropomorphic head phantom using direct digital manufacturing techniques

Silvestre Alberto Piedade

**Mestrado Integrado em Engenharia Biomédica e Biofísica**
Perfil em Engenharia Clínica e Instrumentação Médica

Dissertação orientada por:
Nuno Matela
Geoffrey Mitchel

2020

# Acknowledgments

First of all, my gratitude goes to Professor Geoffrey Mitchel, for giving me the opportunity to work at the Centre for Rapid and Sustainable Product development in the Imaging a Better future project.

Furthermore, Professor Nuno Matela also has my gratitude, since it was through him that I learned about this project. He was always reachable and prompt to help, support and provide feedback whenever required. He has helped me path my future and I hope I can always count on his guidance.

I would like to thank all my colleagues in both IBEB and CDRSP for the warm welcome and all that you taught me in this past year. I could not have made it without you.

I would like to express my deepest gratitude to the Professors of the Institute of Biophysics and Biomedical Engineering for all the time, sympathy, encouragement and knowledge.

A special thank you to my parents and siblings for all their support, not only during this past year but all others as well. Without them this journey would not have existed.

Finally, the warmest “BOAS!” to all my friends, both old and new. You have made this journey all the more exciting and I am truly grateful for all your support.

# Abstract

Positron emission tomography images are used to obtain *in vivo* qualitative measurements of physiological parameters. Partial volume effects, by effectively blurring the images, harms this quantitative nature.

Phantoms can be used to both evaluate how blurred are the images produced by a positron emission tomography system as well as correct for them, by providing a way to obtain a function that maps how this blur across the images. This function can then be used to remove partial volume effects artifacts.

The aim of this study was to develop an anthropomorphic head phantom, with brain and skull structures, to help with the aforementioned tasks, since it will provide a more accurate simulation of real subjects. To build a phantom with structures as complex as grey and white matter and the skull, 3d printing techniques were used.

The models were obtained from magnetic resonance images using seeded region growing algorithms. The segmented models obtained had the basic structure of the target tissues except for the grey matter model which ended up incomplete. Due to this and failure to design a robust brain phantom we were only able to print the cranium portion of the head phantom, and due to the very long print time required, even of this only a small part was printed.

This is the beginning of the project and although a full phantom has not been created we showed that, after some optimizations, it is viable to print a realistic skull phantom, using a polycaprolactone-hydroxyapatite misture that mimics bone's radiological properties.

**Keywords:** PET-CT; Head Phantom; Segmentation; 3d Printing.

# Resumo

Imagens de Positron Emission Tomography (PET) são obtidas detetando a distribuição e concentração de um radiofármaco nos tecidos de um sujeito. Radiofármacos são moléculas que no organismo se comportam de modo semelhante a alguma outra molécula que participe num processo fisiológico, de modo a que estas possam tomar o seu lugar. Em adição, são dopadas com elementos radioactivos de modo a que a sua distribuição monitorizada. Ao escolher um radioisótopo somos então capazes de quantificar o processo fisiológico no qual este participa. A glucose, por exemplo, é utilizada para quantificar a intensidade de procesos metabólicos. Os radioisótopos irão emitir positrões que irão interagir com os tecidos para gerar um par de fotõs que irão viajar em direções opostas. Durante o processo de construção da imagem são as deteções destes pares de fotões que são utilizadas.

Ao atravessar um meio, existe uma probabilidade destes fotões serem absorvidos. Quanto mais denso o meio, maior esta probablidade. No corpo humano, ao cruzar estruturas mais ou menos densas, ossos e pulmões, por exemplo, a quantidade de eletrões atenuados irá variar, distorcendo as imagens geradas. Ao fazer um scan de Computed Tomography (CT), podemos obter um mapa da atenuação das estruturas que é utilizado para corrigir estes efeitos.

Efeitos de volumes parciais (PVE) fazem com que as imagens geradas pareçam algo desfocadas. Estes efeitos têm 2 origens: 1) Como os positrões emitidos pelos radiofármacos têm sempre de atravessar alguma matéria até originarem o par de fotões que será detetado. Até uma distribuição pontual de radiofármaco será observada como um volume. 2) Como os sensores têm uma resolução espacial limitada, os píxeis correspondentes a fronteiras entre duas estruturas irão conter informação misturada das duas. Isto faz com que as fronteiras entre regiões não sejam tão nítidas.

Para vários tratamentos é importante avaliar quantitavimanente certos parâmetros fisiológicos. Por exemplo, é possível avaliar a resposta de um tumor a tratamentos atrávés da sua taxa metabólica, que podemos quantizar com imagens de PET. Infelizmente efeitos de PVE, afetam a precisão destas medidas, ao desfocar as imagens. Torna-se então importante estudar estes efeitos, como os reduzir e avaliar o seu efeito nos vários sistemas de imagem.

Para testar e avaliar a qualidade das imagens geradas por equipamentos PET e o quão fielmente representam a realidade são usados fantomas, objectos que tentam representar o corpo humano, de modo a evitar a exposição de pacientes a estes processos desnecessariamente. Existe ainda a vantagem de sabermos exatamente o resultado esperado para as imagens. Regra geral, estes fantomas correspondem a versões muito simplistas da realidade, recorrendo a formas geométricas simples como retângulos e esferas. O objectivo deste trabalho é desenvolver um fantoma antropomórfico, com estruturas realistas, do cérebro e crânio utilizando tecnologias de impressão 3d para avaliar a performance de equipamentos de PET/CT.

Para obter modelos realistas que podemos passar a uma impressora 3d recorremos à segmentação de imagens de ressonância magnética e CT utilizando algoritmos *seeded region growing*. Estes algoritmos pegam num ponto inicial (semente), com o qual comparam os valores dos píxeis vizinhos. Caso

a diferença de intensidades entre os píxeis vizinhos e a média da região que está a ser segmentada seja menor que um limite pré-definido, estes são acrescentados à região segmentada. É através deste limite e das sementes iniciais que variamos os resultados da segmentação. Este algoritmo em particular adequa-se a esta tarefa uma vez que as regiões correspondentes às matérias branca e cinzenta têm contornos complexosmas com baixa variação de intensidade dos píxeis no seu interior.

Tentámos aplicar o mesmo algoritmo para segmentar o crânio e o cérebro. Devido à estrutura do osso do crânio, esponjoso (logo menos denso) no centro fomos capazes de segmentar o seu contorno corretamente à custa de uma maior espessura deste. Quanto ao cérebro, apesar da matéria branca e ventrículos terem sido corretamente segmentados, a matéria cinzenta, que neste contexto pode ser vista como uma camada ao redor da matéria branca, possui várias zonas onde é inexistente. Nestas, ou se apresenta como matéria branca ou não existe de todo.

Utilizámos os modelos da matéria branca e cinzenta para remover o excesso do modelo do crânio e, de seguida, dividimos este modelo em múltiplas peças que a impressora à nossa disposição é capaz de imprimir. Para o fantoma do cérebro tentámos apenas recriar uma região oca correspondendo à matéria cinzenta. Para tal dilatámos o modelo da matéria cinzenta, de modo a obter a parede exterior deste e utilizámos o modelo da matéria branca para obter a sua parede interior. Esta abordagem gerou uma câmara oca correspondente à matéria cinzenta com uma espessura muito inferior ao esperado e que, em certas regiões era até inexistente (devido aos modelos utilizados). Um problema maior, no entanto, é que esta abordagem não teve em conta a robustez mecânica do fantoma, não tendo estruturas de suporte nem podendo garantir uma forma eficaz de encher e vazar o fantoma com os radiofármacos de modo a testá-lo. Assim sendo apenas avançámos para a fase de impressão 3d do modelo do crânio.

De modo a que o fantoma do crânio se comporte de modo semelhante ao osso (em relação às suas propriedades imagiológicas), criámos uma mistura de policaprolactona (PCL) e hidroxiapatita (HA) em proporção de 50%.

Para imprimir a peça utilizámos uma impressora 3d feita por medida que nos permite personalizar os materiais com os quais queremos imprimir. Utilizámos um bocal de $0.3mm$ que apesar de permitir maior detalhe exige um grande número de passagens para gerar cada camada da peça. Estimámos que, para imprimir todas as peças do crânio, demoraríamos cerca de 5 meses pelo que apenas imprimimos uma única parte. A peça que imprimimos demontra que é possível utilizar a impressora BIOMATE para este tipo de trabalhos uma vez que mesmo sem material de suporte fomos capazes que obter estruturas como arcos e rampas, necessárias para a impressão de estruturas complexas, apesar de ser necessário referir que não de forma perfeita. Será necessário continuar a optimizar o processo, em particular tentar minimizar deformações geradas enquanto camadas já impressas arrefecem durante o processo de impressão.

Apesar de não termos concretizado todos os objetivos a que nos propusémos temos agora uma ideia melhor de onde concentrar os nossos esforços: Obter boas imagens nas quais basearemos a segmentação; Perceber a melhor forma de passar de um modelo do cérebro para uma estrutura oca do fantoma que permitirá o fluxo de radiofármaco e Possiveis formas de expeditar o processo de impressão.

**Palavras-chave:** PET-CT; Fantoma da Cabeça; Segmentação; Impressão 3d.

# Contents

# List of Figures

# List of Tables

# List of Acronyms

**CAD** Computer Aided Design 1, 9, 11

**CAM** Computer Aided Manufacturing 1, 9

**CNC** Computer Numerical Control 1, 9

**CSF** Cerebrospinal fluid 1, 13

**CT** Computed Tomography vii, 1, 2, 4, 5, 7, 11, 13

**FDM** Fused Deposition Modeling 1, 9, 10

**HA** Hydroxyapatite 1

**MRI** Magnetic Resonance Imaging 1, 11, 13–15

**NEMA** National Electric Manufacturers Association xi, 1, 6, 7

**PCL** Polycaprolactone 1

**PET** Positron Emission Tomography vii, xi, 1–3, 5–7

**PVE** Partial Volume Effects 1, 2, 5

**SL** Stereolitography 1, 9, 10

# Chapter 1

# Context and Outline

## 1.1 Introduction

The concept of personalized medicine has been around for some time although it is only more recently been gaining increased focus [1]. Fundamental to it is medical imaging which has not only been, in a way, always personalized, but is also fundamental in the process of planning and adjusting medical interventions to each patient and follow up procedures. There are two main imaging types: anatomical and functional. Anatomic imaging provides us insight into the structure and organization of our internal organs while functional imaging gives us information on the metabolic activity of physiological and pathological processes. PET belongs to the latter category and will be the target of our focus.

PET imaging is useful in *in vivo* quantitative assessment of molecular targets in a wide range clinical applications. In oncology it is used to assess the tumor metabolic activity and track its evolution during treatment as well as in diagnostic, staging and monitoring the disease. In neurology it can be used to create maps of normal versus abnormal brain function and diagnose some dementias.

Its quantitative potential is still hampered by several physical degrading factors, in particular, Partial Volume Effects (PVE) that arise from poor spatial resolution that spreads the same uptake over a larger volume [2], and photon attenuation, when these cross denser tissues, like bone, resulting in an overall decreased activity in the final image. For the particular case of assessing the response to therapy, increased certainty is needed due to the stacking of errors that will occur when repeatedly scanning the same patient for the duration of the treatment to track its progression. There is also the fact that during treatment the lesion will become progressively smaller, making PVE more relevant.

Imaging phantoms are objects designed to evaluate and/or tune the performance of medical imaging systems. These are usually more readily available and provide more consistent results than living subjects, thus allowing for more rigorous comparisons between different systems, while avoiding exposing subjects to unnecessary risks, usually radiation. The design of a phantom depends on its purpose and currently accepted imaging phantoms used to assess the imaging systems', such as CT, PET and Magnetic Resonance Imaging (MRI), performance usually consist of a collection of geometric shapes, like grids, ramps and spheres, that allow the measure of relevant image quality parameters, like spatial resolution, contrast and signal to noise ratio.

Although these phantoms produce consistent measures, useful for routine maintenance, they may not always directly translate into better real-world performance. To account for this, anthropomorphic phantoms have been developed containing more complex structures that mimic the human anatomy more accurately. This also makes them harder to build, the Hoffman phantom , for example, requires the assembly of several individually machined pieces [3]. Fortunately a technology that can be used to

assemble such complex structures while remaining relatively inexpensive, direct digital manufacturing, or 3D printing as it is more commonly known, exists, with some attempts at using it to assemble phantoms already being researched [4].

## 1.2 Objectives

The goal of this master's dissertation is to design and build, using 3D printing techniques, an anthropomorphic brain phantom that can be used to evaluate the performance of PET/CT imaging systems, more specifically with regards to PVE.

## 1.3 Outline

This work was a collaboration between the Institute of Biophysics and Biomedical Engineering (IBEB) and the Centre for Rapid and Sustainable Product Development (CDRSP). In IBEB we worked on the image processing necessary to obtain the models for the phantom design while in CDRSP we dealt with the 3d printing process, from the design constraints related to it to the materials used.

In the following chapters we will go over the concepts necessary to understand this work. We begin, in chapter 2, by looking into PET imaging systems, from basic principles to quality assurance methods and some of the phantoms used for such, followed by an overview of the 3d printing technologies that may be employed to built a phantom, in chapter 3. We then look into the image processing methods used for both pre-processing and segmentation of the images with which we will build our phantom in chapter 4. Finally, we will review our approach to the problem at hands and the results obtained in chapters 5 and 6, respectively.

# Chapter 2

# Principles of Medical Imaging

Many technologies have been developed that give us an insight on the interior of the human body. We will be focusing on Positron Emission Tomography.

## 2.1 PET Imaging Principles

PET is a medical imaging technique that allows quantitative *in vivo* measurements of 3d distributions of positron-emitting tracers. Depending on the tracer used it can measure several physiological parameters, such as glucose and oxygen consumption or drug delivery and uptake values.

PET images are obtained by detecting a very small amount of radio-tracer that is administered to the patient to be distributed among and within the target organs [5]. The radiotracer emits positrons that travel up to several millimeters through tissue until they collide with an electron and generate a pair of photons that travel in near opposite directions with an energy of $511KeV$, see figure 2.1. The detection of these pairs is fundamental for the image acquisition process, where millions of detection are being made and filtered for coincidences that are then mapped during image reconstruction to provide the distribution of radio-tracer in the tissues. Several factors contribute to the final result of a PET scan, we will be focusing on photon attenuation, and its correction, and partial volume effects.

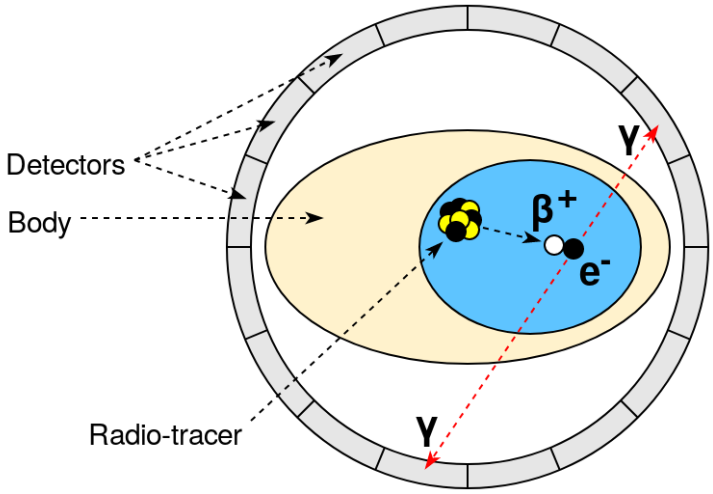


Figure 2.1: Here we have a simplified model of a PET system: the radio-tracer (yellow and black) will emit a positron ($\beta^+$) that when combined with an electron ($e^-$) will generate a pair of photons with $511KeV$ each ($\gamma$). If two sensors detect these photons at the same time then the event is registered and the line of response (dashed red arrow) is saved to be used during image reconstruction.

### 2.1.1 Attenuation correction

Photon attenuation inside the patient causes a large fraction of the photons to not reach the detectors. Fortunately, this attenuation does not depend on their location in the line of response, and by acquiring a CT scan of the patient we can correct this effect. An important concept to have in mind when dealing with attenuation correction is the *linear attenuation coefficient*, used to characterize how easily a volume of material can be penetrated by a beam of energy/matter (fig. 2.2). A large coefficient means that the beam is quickly attenuated as it passes through the medium while a smaller one means that it will be more transparent to it.

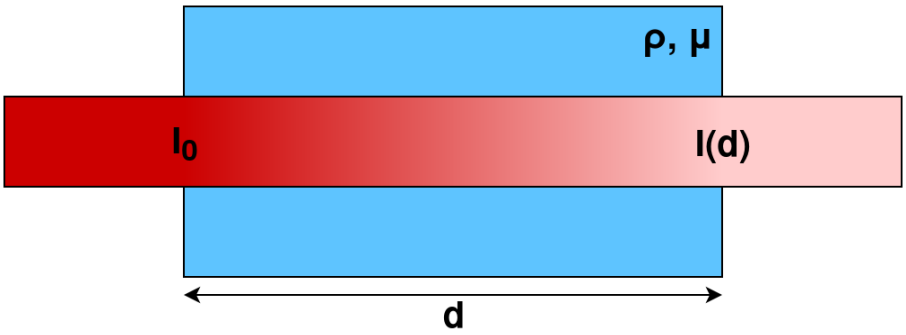


Figure 2.2: In this figure we can see a simplification of an intensity profile of a beam, in red, across a medium, in blue. As we can see as the distance crossed grows, the beam energy (represented by its color intensity) decreases.

We can employ the following expression to calculate the intensity profile of, in this case, an X-ray beam across a medium:

$$I(x) = I_0 e^{-\mu x} \tag{2.1}$$

where $I(x)$ is the beam intensity at $x$ , $I_0$ is the initial beam intensity, $\mu$ is the attenuation coefficient with SI units of $[m^{-1}]$ and $x$ is the distance traveled across the medium. When employing this expression we might also frequently use the *mass attenuation coefficient* $(\mu/\rho)$ multiplied by the medium's density $(\rho)$:

$$I(x) = I_0 e^{-(\frac{\mu}{\rho})\rho x} \tag{2.2}$$

We can calculate the mass attenuation coefficient of a mixture with:

$$\frac{\mu}{\rho} = \sum_{n=0} (\frac{\mu}{\rho})_n w_n \tag{2.3}$$

where $(\frac{\mu}{\rho})_n$ and $w_n$ are the mass attenuation and weight fractions of the $n^{th}$ element, respectively.

In CT imaging instead of the attenuation coefficients of each tissue, the metric used for radiodensity are the *Hounsfield Units* (HU). This scale is based on the attenuation coefficients of distilled water and air, corresponding to 0 and $-1000$ HU, respectively, with objects denser than water having positive values. We can go back and forth between Hounsfield units and the attenuation coefficient using

$$HU = \frac{\mu - \mu_{H_20}}{\mu_{H_20} - \mu_{air}} 10^3 \tag{2.4}$$

where $\mu_{H_20}$ and $\mu_{air}$ are the linear attenuation coefficients of water and air, respectively.

Photon attenuation leads to the loss of counts of some photons across denser paths which may hurt

image quality. To correct this, a CT scan can can be made of the subject or object we want to image, where we obtain a map of the tissues' attenuation coefficients. With these maps we can later, artificially, increase the number of detections along the lines where tissues have greater attenuations.

### 2.1.2 Partial Volume Effects

PET is intrinsically quantitative with indices like the standard uptake value (SUV) allowing us to move away from subjective analyses of medical images [6]. This quantification derives from the used radiotracers that are biologically active molecules with a positron-emitting atom. By choosing different molecules we can target specific physiological processes and quantify how active they are since higher physiological activity increases the local concentrations of the necessary molecules (that we have marked with the radioisotopes) which finally into a brighter zone in the final PET image.

When measuring tracer uptake in small tumors, PVE might introduce large biases in our measures, harming the quantitative nature of the image. There are two contributing phenomenon to PVE [7]. The first one comes from the limited spatial resolution of the detectors which leads to a "spill out" of some radiation that will appear outside its actual source (fig. 2.3a). The second phenomenon is caused by image sampling, due to the mismatch of voxel and organ contours, where the signal intensity of a voxel corresponds to the mean of the signal intensities of all the tissues that belong in it (*Tissue fraction effect, figure 2.3b*).

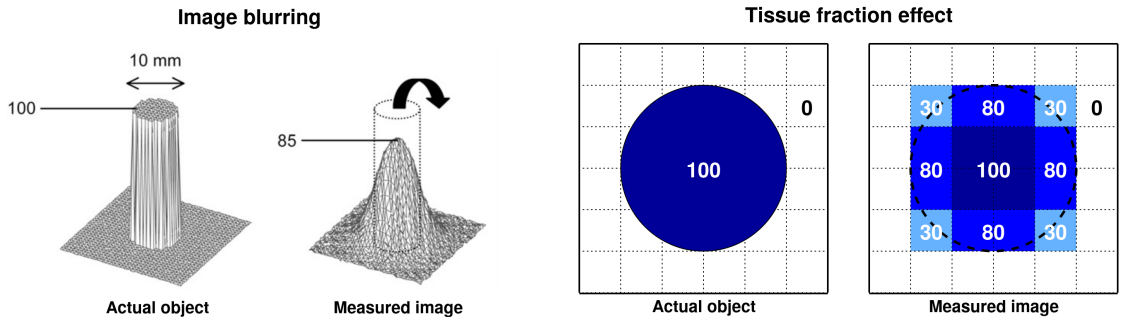


(a) (b)

Figure 2.3: Image blurring effects happen when a point source is diffused over a larger area, a), while tissue fraction effects, occur when two sources with different intensities are forced to share the same voxel/pixel, b). In the case of a frontier between two organs with different activities this results in the diffusion of its intensity throughout the shared voxel.

PVE spreads the signal of a hot region that lies in the middle of a cold one. This usually occurs when the tumor size is 3 times smaller than the *full width at half maximum* (FWHM) of the reconstructed image and in such instances small tumors will appear larger but less aggressive than they are [7]. PVE does not eliminate any signal, it simply scatters it over the image.

By using phantoms or other, more specific point-sources for which we have precise locations and sizes, we may use the resulting images to calculate a point spread function representing the blur generated by PVE. We can then deconvolute the images with this function to deblur them [8].

## 2.2 Quality Assurance

To prevent defects in the imaging systems and ensure the safety of both the patients and healthcare professionals we need to have well implemented quality assurance programs. These serve several pur-

poses:
• Ensure than an imaging system works as specified. Both hardware and software wise.
• Establish a baseline performance against all future quality tests will be compared.
• Provide data that helps to determine optimal operation parameters.
• Ensure the equipment meets radiation safety regulations.

Sometimes two similar concepts - *acceptance testing* and *quality control* - can be found. They are very similar with the main difference being when the processes described bellow are executed: Acceptance testing is applied when acquiring a new system while quality control relates to measuring the system's compliance with the tests throughout it's useful life span.

Many standards have been developed to achieve this task [9, 10, 11]. The NEMA standard [9] utilizes five parameters to assess a PET system's performance: **Spatial resolution:** tests the system's ability to distinguish between two points after image reconstruction.
**Scatter fraction, count losses and randoms measurements:** This parameter assesses the system's ability to measure highly radioactive sources.
**Sensitivity:** tests the minimum activity that the sensors can detect. It also closely relates with the next parameter;
**Accuracy:** that measures the number of *true detections*, that can arise from several different factors that PET systems must try and compensate such as dead time losses and random detection events.
**Image quality, accuracy of attenuation, and scatter corrections:** To obtain this measurement we simulate a whole-body imaging scan with hot and cold regions providing a simulation of a (limited) real world situation. Image quality is assessed by calculating image contrast and background variability ratios for the hot and cold regions. This test also measures the accuracy of attenuation and scatter correction and quantification of radioactivity concentration in the volume of interest.

Most of these provide a metric on the best possible value using a situation that will never occur in a clinical environment, like the spatial resolution test that requires point sources. The image quality test, on the other hand, tries to emulate a real world use case, using hot and cold regions with different sizes and a compartment to simulate the attenuation. This is the test we aim to improve with a more realistic phantom.

We will now review some of the phantoms used for these tests and some attempts at creating anthropomorphic head phantoms. After getting to know the NEMA image quality phantom we will briefly go over how it is used to measure image quality.

## 2.3 Phantoms

Phantoms are objects that try to represent the human body whose design and composition are determined by their purpose. Imaging phantoms are used to study the image quality and performance of the systems and new algorithms as well as performing routine quality control without exposing any patients to unnecessary doses of radiation. They need to be built so that either their materials have the same imaging properties of human tissues or with compartments that can be filled with materials that do.

The NEMA image quality phantom [12] in figure 2.4a is a well known phantom that tries to mimic the human upper body shape. It is built of acrylic glass, contains 6 hollow glass spheres that can be filled with radiotracer to emulate hot regions and a central cylindrical insert that is filled with styrofoam to simulate lung attenuation. An example of an image generated by scanning this phantom is shown in figure 2.4b.

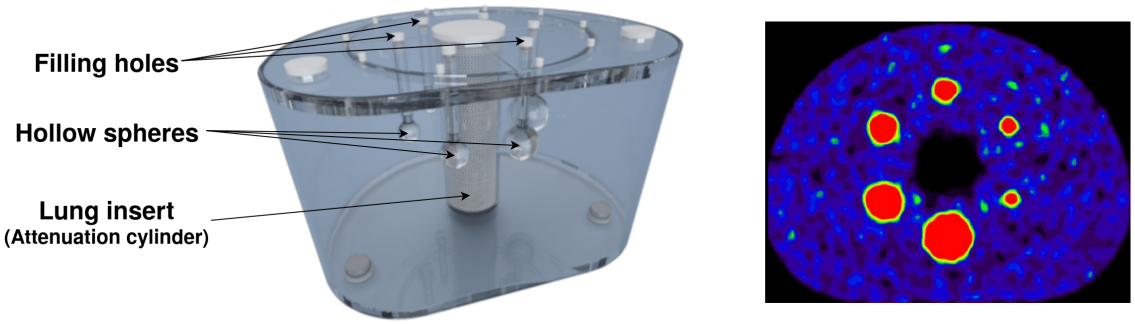


(a) (b)

Figure 2.4: In this image we show an image of the NEMA phantom, a), and the images obtained with it, b). Image adapted from [13].

Image quality with this phantom is assessed by choosing a transverse slice of the reconstructed image, and utilizing the hot and cold regions to calculate the contrast between them. To test the attenuation correction accuracy a region of interest (ROI) around the lung insert is selected and its attenuation coefficient is compared to the expected one of styrofoam.

When evaluating the accuracy os PET/CT systems there is a gap between the images obtained from phantoms with simple geometric shapes and the ones with *in vivo* activity distributions. Several attempts at designing anthropomorphic phantoms have been made.

An earlier attempt resulted in the Hoffman phantom [3], built out of stacked layers of machined plastic sheets with two different combinations: thick and thin, shown in figures 2.5a and 2.5b, respectively. Both layers follow the same design concept where the zones corresponding to either grey or white matter are hollowed out to make space for the radiotracer containing fluid. The different slice thickess has the purpose of differentiating between grey and white matter by creating a 5 to 1 ratio in “grey” and “white” matter in the phantom (grey matter is represented in the thicker slices). All the slices are stacked together as shown in figure 2.5c.

More recent attempts at constructing realistic phantoms employ 3D printing technologies that allow for more complex shapes without much of the extra work previously associated with them. One such attempt is the phantom designed by Iida *et al* [14] that contains both bone and grey matter structures. This phantom’s core design is similar to the hoffman phantom, with the main differences being the existence of bone mimicking material*, representing the skull, the outer shape of the phantom, that is a head instead of a mere cylinder, and the slices that were 3D printed instead of machined.

We are now going to review a couple of the currently existing 3D printing technologies.

*Throughout this text when we state we are mimicking bone, we are referring to its imaging properties, not mechanical.

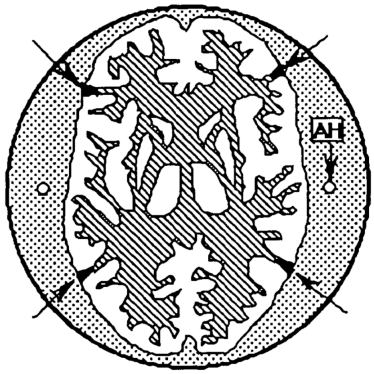


(a) Thick layer

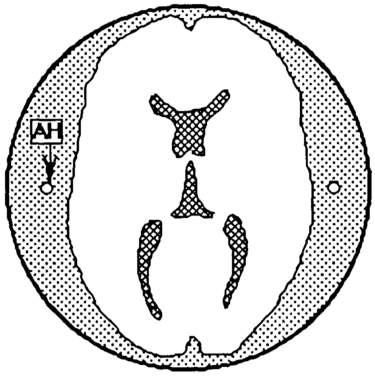


(b) Thin layer

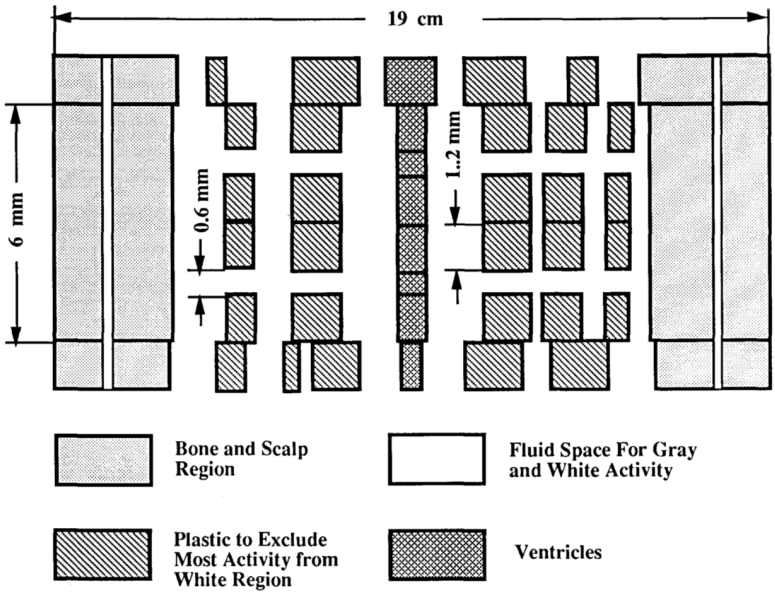


(c) Layer assembly

Figure 2.5: On the top of this figure we can see the cut outs of the thick (a) and thin (b) layers. Marked with "AH" are the alignment holes, used to keep all pieces in place when they are being assembled together. The unlabeled arrows in (a) denote artificial structures that were added for support. In (c) we can see a slice across all the pieces and how they fit together to form the interior cavities of the phantom. These images were taken from [3]

# Chapter 3

# 3D Printing

3D printing, is a branch of Computer Aided Manufacturing (CAM), which uses software and computer controlled machinery to automate the manufacturing process. 3D printing is based on additive processes where an object is created by sequentially printing its cross sections until the object is complete [15]. There are two different types of software necessary for CAM, the one used for drawing and optimizing the object's design, aptly named Computer Aided Design (CAD) software, that outputs the digital files necessary to print the schematics and 3D printing or machining. The second class of software needed is the one responsible for controlling the automated machining tools and 3D printers, named Computer Numerical Control (CNC) software.

This chapter aims to review the two 3D printing techniques we had available.

## 3.1 Stereolitography and Fused Deposition Modeling

The two 3D printing technologies we have available are Fused Deposition Modeling (FDM) and Stereolitography (SL). Their main differences arise from the way new layers are added: In SL (see fig 3.1), each layer comes from the cure of a photosensitive polymer using an ultraviolet laser that promotes the cross-linking of monomers into polymers, turning it from liquid to solid. By using a laser to control where the resin is hardened, this process achieves better spatial resolutions (finer details and a smoother finish), although at the cost of a more limited range of materials, that need to be resin based.

FDM (figure 3.2), on the other hand, directly extrudes a thin filament of polymerizable material that has been partially melted on top of the previous layers, that adhere to each other, forming a solid piece after it all cools down. The advantage of this method is the greater variety of available materials that may even contain iron powder to give them ferromagnetic properties or a sawdust mixture for a wood-like finish. Sometimes, a heated base is used to prevent the bottom layers from cooling too quickly while new ones are still being added in order to prevent the object from warping.

One of the printers available in CDRSP, the BioMaTe 3D printer (figure 3.3), was custom made, in-house, to accept pellets of material instead of filaments. Thus, we can create small batches of custom materials, that are not or may never be available otherwise.

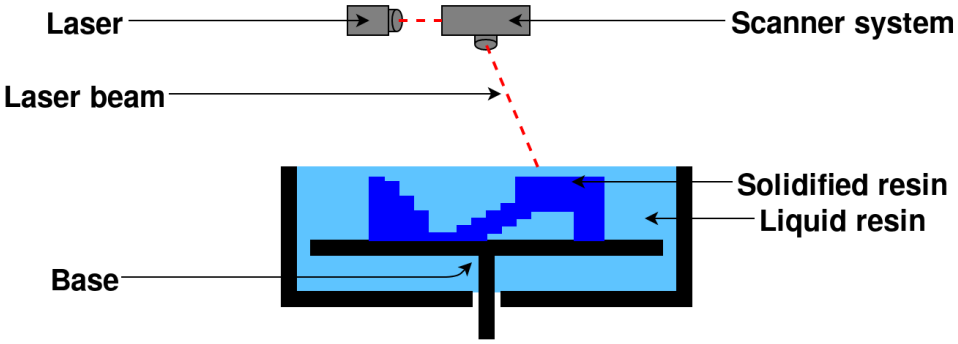


Figure 3.1: Here we can see a simplified version of how a SL printer works. Resin is poured into a container where the base rests on top of a piston. A laser beam is generated and directed by a scanner system so that it shines on the resin on the appropriate places. After each layer is set, the base is lowered and the resin container might be rocked back and forth to make new resin cover the printed layer. Some systems might be found where the setup shown is inverted with the layer shining from bellow and the base rising out of the resin.

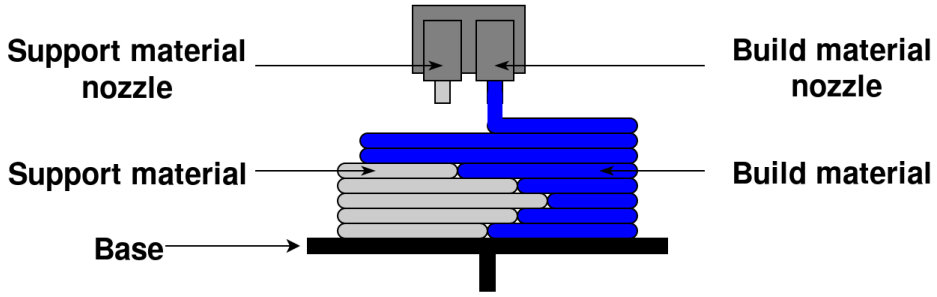


Figure 3.2: In this figure we present a simplified FDM printer. The one shown contains two nozzles but most may contain only one while others might have more. These extrude material (never at the same time), layer-by-layer. Unlike SL, in FDM the fixed part is the base and what moves up and down is the platform that supports the extruders.

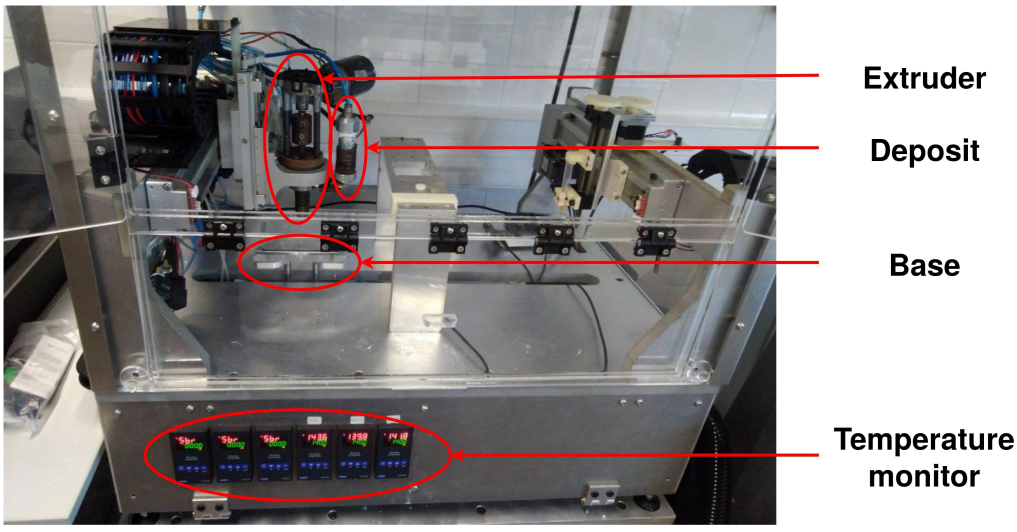


Figure 3.3: Here we have the BioMaTe 3D printer. We can see the deposit where we introduce our pellets, and the extruder that outputs them to the base. The extruder moves only on the y axis, while the base moves on the x and z, to achieve 3 degrees of movement. The temperature monitor allows us to track the temperature on the regions between the deposit and extruder.

## 3.2 3D Printing of Realistic Phantoms

In order to print accurate organ models we cannot simply input medical images into a 3d printer. We first need to segment these images and, using CAD software, generate the files that the 3D printers can interpret [16, 17].

The anatomically accurate models we are aiming for can be generated based on medical imaging data, like CT or MRI that are used to obtain images of either the full body or only specific areas of interest. These imaging modalities highlight different tissues and/or features: CT images are highly dependent on tissue density to generate contrast and, as such, are useful to segment either high or low density structures, like bones and lungs, respectively, while MRI offers great soft tissue contrast, making it useful for differentiating grey and white matter. Many software packages are readily available that allow us to more-or-less automatically segment images [18, 19].

Depending on the structures we are trying to mimic with our phantoms we may need to replicate not only the correct shape, but also print it using the appropriate material. For instance: in the brain phantom what is mimicking the brain tissues is the liquid containing the radiotracer which means we only need to focus on printing the right container shape while for bone we should print the phantom itself with a material that mimics its properties [20].

In the next section we are going to review some of the algorithms implemented in these packages that will ultimately allow us to move from anatomical images to 3d printable models of organs.

# Chapter 4

# Image Processing

Like stated in the previous chapter, to 3d print any object we first need the model of each individual part or just the whole of it. To obtain realistic organs we will derive the models from real anatomical images, utilizing image segmentation algorithms.

Image segmentation is the process of partitioning an image into multiple segments (or objects). In one of our use-cases it will, for example, take MRI images that contain all brain structures connected to each other and separate them into various models containing grey matter, white matter and Cerebrospinal fluid (CSF).

To improve the performance of these algorithms we must first pre-process our images, in order to filter some of the noise and artifacts that may be present. As such we will begin by reviewing the pre-processing methods employed, followed by the segmentation algorithms themselves.

## 4.1 Pre-processing

We will be dealing with two kinds of medical images: CT and MRI, for the segmentation of bone and brain structures, respectively. Due to the different natures of each image, they may require different algorithms. CT images required a minimal amount of pre-processing while MRI images required a more sophisticated approach.

### 4.1.1 Median Image Filter

Median filters are used to remove noise while preserving any edges present in the images, which is an important detail if we are to employ a region growing algorithm in the segmentation stage. These filters remove noise without altering any edges present, effectively smoothing out the intensities inside each region which will improve the region growing algorithms' performance.

This algorithm works by replacing each image pixel intensity with the median value of its neighborhood [21]. We used the SimpleITK.MedianImageFilter() function of the SimpleITK python module. The only arguments it accepts are the neighborhood radius and the image.

### 4.1.2 Bias Field Correction

The bias field is a low frequency intensity nonuniformity present in MRI images that arises from nonuniformities in the magnetic field during acquisition, see figure 4.1. Although for someone doing manual segmentation this doesn't present significant problems, for automatic algorithms that deal with precise intensity values even the slightest deviation will lead to errors in the end results.

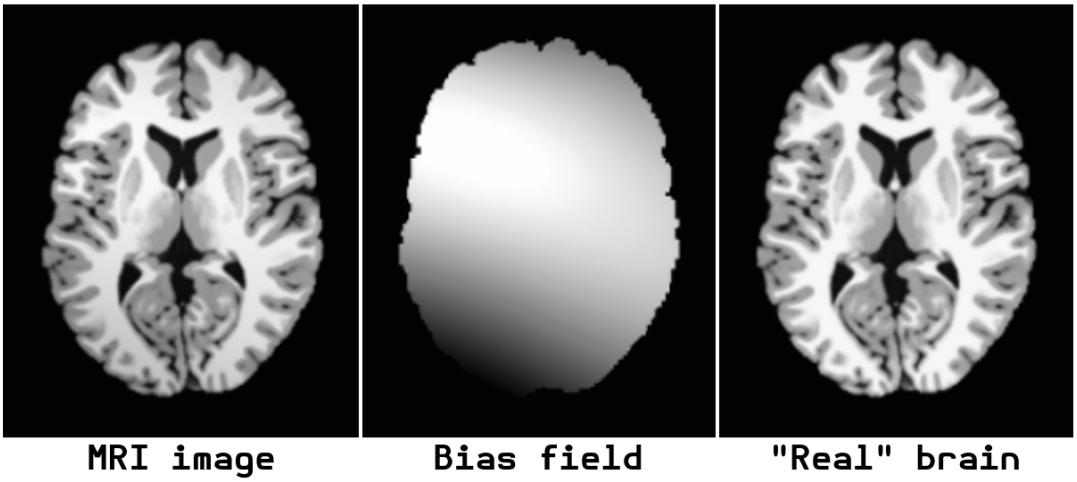


Figure 4.1: On the left we show an unprocessed MRI image. Notice how the color varies smoothly across the image due to the bias field, shown in the middle. By subtracting one from the other we obtain an image with minimal variation of pixel intensities within each structure like shown on the right.

If we represent the measured image with $v(\mathbf{x})$, the true image with $u(\mathbf{x})$, the bias field with $f(\mathbf{x})$, and random Gaussian noise with $n(\mathbf{x})$, as in [22], all variables can be correlated with:

$$v(\mathbf{x}) = u(\mathbf{x})f(\mathbf{x}) + n(\mathbf{x}) \tag{4.1}$$

which, with $n = 0$ and $\hat{a} = \log a$, can be rewritten as:

$$\hat{v}(\mathbf{x}) = \hat{u}(\mathbf{x}) + \hat{f}(\mathbf{x}) \tag{4.2}$$

To determine the bias field, based on these images, we will be using the N4ITK bias field correction algorithm [22] that iterates the "real" image estimation with:

$$\hat{u}^n = \hat{u}^{n-1} - \hat{f}_e^n = \hat{u}^{n-1} - S[\hat{v} - E(\hat{u}|\hat{u}^{n-1})] \tag{4.3}$$

where $S$ is a B-spline approximator, $E(\hat{u}|\hat{u}^{n-1})$ the current estimate of our true image, $\hat{u}^0 = \hat{v}$. *

The B-spline approximator $S$, of order $(n,m)$, is defined by the knot-vectors $\mathbf{U} = \{U_1, ..., U_n\}$ and $\mathbf{V} = \{V_1, ..., V_m\}$, using the Cox-de Boor recursion algorithm:

$$\mathbf{S}(u,v) = \sum_{j=0}^{m}\sum_{i=0}^{n} B_{i,n}(u)B_{j,m}(v)\mathbf{P}_{i,j} \tag{4.4}$$

$$B_{i,n}(u) = \frac{u - U_i}{U_{i+d}}B_{i,n-1}(u) + \frac{U_{i+n+1} - u}{U_{i+n+1} - U_{i+1}}B_{i+1,n-1}(u) \tag{4.5}$$

$$B_{i,0} = \begin{cases} 1, U_i \leq u \leq U_{i+1} \\ 0, otherwise \end{cases} \tag{4.6}$$

where $\mathbf{P}_{i,j}$ are the control points of the b-spline. These are calculated using a least squares approximation

*The variables $u$ and $v$ mentioned before and after this point are not the same. Before, they correspond to the true and measured images while after they represent the B-spline surface parameters.

to the data points $\mathbf{S}(u,v) = \{S_1(u_1,v_1),...,S_k(u_k,v_k)\}$:

$$\mathbf{P} = (B^T B)^{-1} B^T \mathbf{S} \tag{4.7}$$

### 4.1.3 Brain Extraction

MRI images contain a considerable amount of non-brain tissues like eyeballs, skin and fat, see fig 4.2. Segmentation robustness and speed are improved if these are removed beforehand since no compute power is wasted on these.

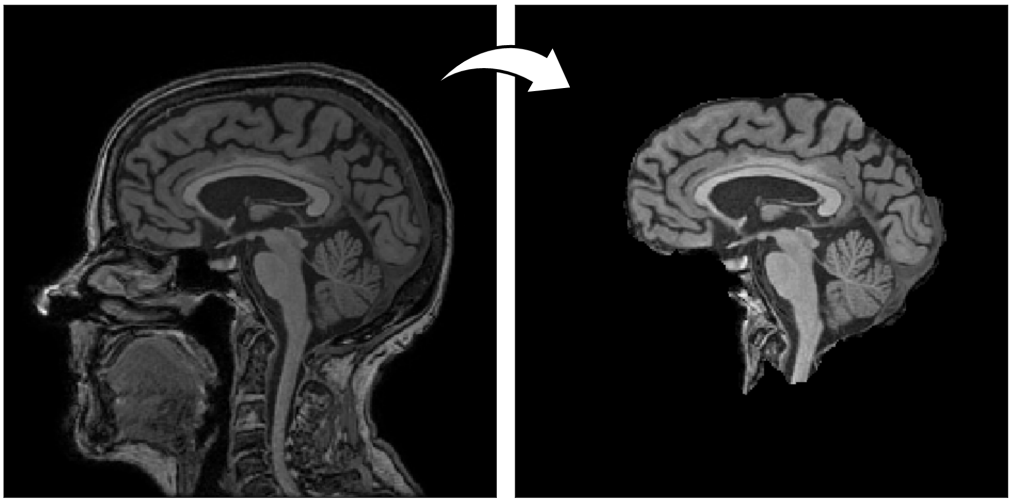


Figure 4.2: On the left we have a full head MRI image that we can verify has a lot of unnecessary tissues. We can simplify the image before processing by removing the unwanted tissues and leaving only the brain like shown on the right.

To separate the brain from the rest of the image we will be using the Brain Extraction Tool (BET) [23]. This tool allows a rough separation of brain and non-brain tissues, returning a mask corresponding to the former. It does so by deforming a tessellated surface until it matches the brain outline.

The algorithm [23] begins by estimating intensity thresholds corresponding to the bottom and top 2% intensity voxels, $t_2$ and $t_{98}$, respectively. It then defines the brain/background threshold ($t$) as being 10% of the way between $t_2$ and $t_{98}$. To obtain the brain's center of mass we use all the voxels with intensity values greater than $t$ and calculate a weighted sum of the positions. Assuming a spherical brain centered around the center of mass the radius that includes all brain pixels (the ones between $t_2$ and $t_{98}$) is calculated. The center of mass and radius are then used to initialize a tessellated surface. A series of iterations follow where each vertex is updated leading to surface getting closer and closer to the brain's shape. The general algorithm is presented in figure 4.3

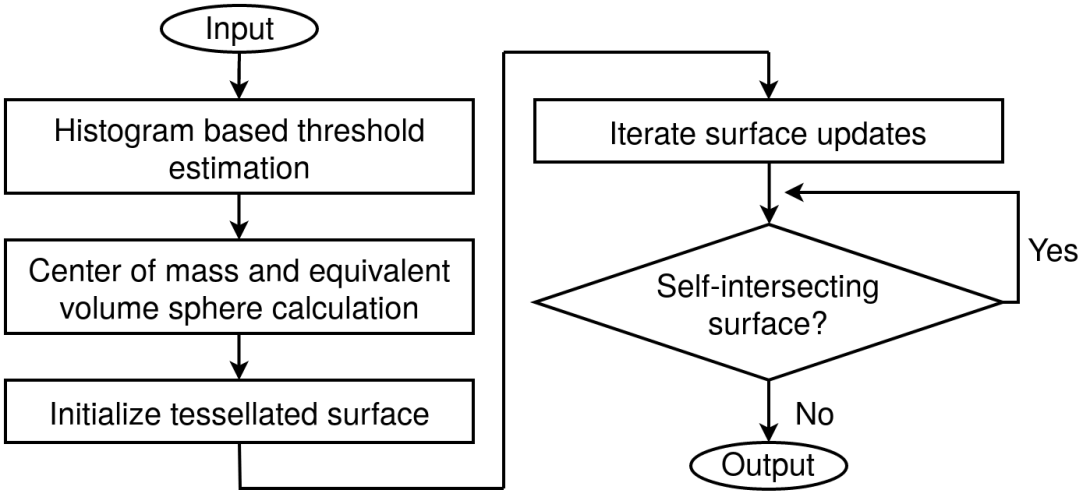


Figure 4.3: BET algorithm flowchart.

### 4.1.4 Morphological filters

Morphological operators may be used to modify regions in an image by convoluting it with a structuring element, or kernel. The simplest operators are dilate and erode, and perform the operations they take their names from. These can be combined into the image open and close operators. The former corresponds to the dilation of the erosion, and enlarges any holes smaller than the structuring element while the latter corresponds to the erosion of the dilation and results in the closure of any holes smaller than the structuring element. In figure 4.4 we show the results of each filter on a simple binary image.

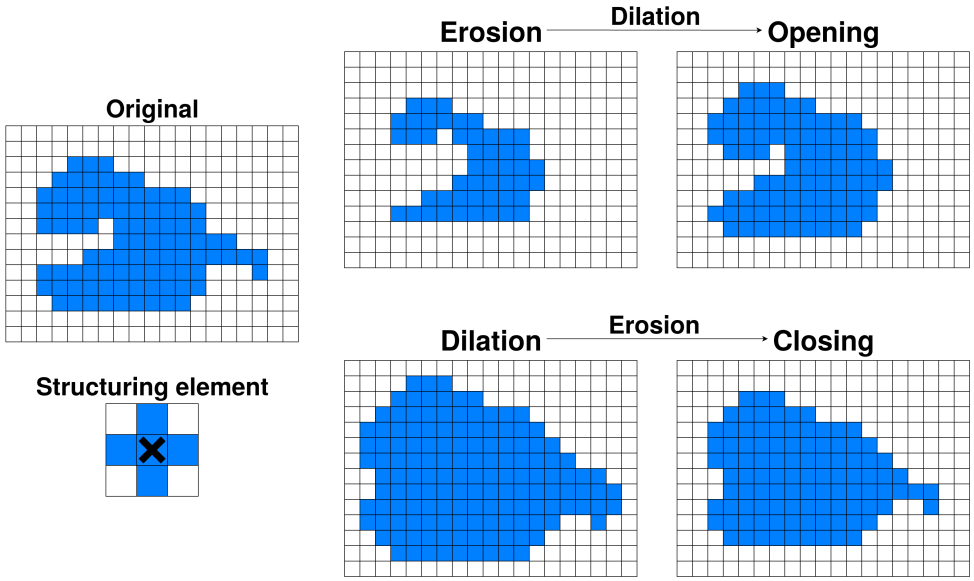


Figure 4.4: In this figure we show-case the four most simple morphological operations. To dilate an image we place the kernel on top of each pixel that belongs to the image and add any elements it touches. To erode an image we take away any element encompassed by the kernel while it swipes through every pixel that does not belong to the image. If we sequentially apply these two operations we will arrive at either the image open or image closing filters, depending on the order they were applied.

Although we are introducing these filters in the pre-processing section we will also use them after segmentation to clean up any small errors.

## 4.2 Segmentation

There are four main approaches to image segmentation: threshold-based, boundary-based, region-based and hybrid techniques.

The 2 methods we'll be reviewing are the threshold segmentation method and the seeded region growing, the later belonging to the region-based techniques.

### 4.2.1 Threshold segmentation

Threshold based methods rely on the assumption that pixels whose intensity values lie in a close range belong to the same class.

Threshold segmentation works by comparing each image element's intensity value to specified limits, the thresholds.

These methods ignore all spatial information.

Depending on the situation, if the intensity value is above, below or in between the specified thresholds it is added to the segmented region.

### 4.2.2 Seeded region growing

Region growing algorithms rely on the assumption that pixels with similar intensity values that share a neighborhood belong to the same region [24].

We will use this algorithm to segment the brain structures because they contain complex contours that this algorithm can easily follow. The algorithm begins with a number of seeds, usually manually selected, that are put into multiple sets $A_0, A_1, ...A_n$. We can select various initial seeds for the same structure in which case they are placed within the same set.

In the next step two distinct operations are performed: For each set, $A_i$, the average intensity, $\mu$, and standard deviation, $\sigma$ are calculated. The neighboring pixels of each set are placed in separate sets. For 2d region growing, either 4 or 8-connected neighborhoods can be used, figure 4.5. The algorithm we will be using for 3d region growing utilizes a 26-connected neighborhood [25].

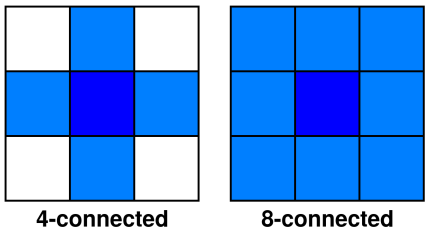


Figure 4.5: In this figure we compare two types of pixel connectivity. 4-connected (left) and 8-connected (tight). For 2d images these are the simplest neighborhoods and can easily be extended to 3d by going from a 3x3 square to a 3x3x3 cube whose vertices would or would not count towards the neighborhood for the 6 or 26-connected cases.

We then use these values to determine if the neighboring pixels should belong to this region: If a neighbor pixel's intensity lies in the interval $[\mu - c\sigma, \mu + c\sigma]$ then it is added to the corresponding set $A_i$. The constant $c$ controls how much a pixel is allowed to differ and still be considered part of the group and is one of the values used to tune the algorithm's behavior.

Each iteration of the algorithm will repeat these steps. We calculate each set's average intensity and standard deviation, find its neighbors and compare them to the set. The algorithm stops when no more

neighbors are found or the sets stop growing.

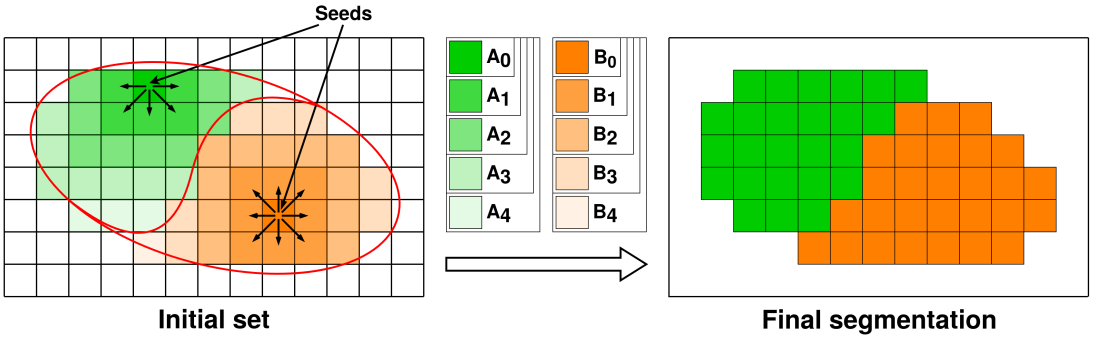


Figure 4.6: The arrows indicate the direction of growth of each set on the first iteration. The shaded colors were used to help visualize the size of each set on each iteration. The final result of the simple image is presented on the right. in this example by adding more seeds we could take the number of iterations down to half. In a real case due to the dimensions of the image adding more seeds would not have this impact on the number of iterations.

## 4.3 Marching Cubes

We are currently able to segment objects, but they are still only a set of voxels that must be converted to surfaces in order to be 3d printed. We do it with the marching cubes algorithm [26, 27].

To easily understand the principles of this algorithm we will use its 2d analogue, aptly named the marching squares algorithm. Since we are working in 2d the result of this algorithm will not be a surface but a contour.

We begin by placing a grid with the vertices that coincide with the center of the image pixels. Each vertex is then tagged as being inside or outside the object. We then "march by" each cube, matching it against a lookup table that contains all possible contour segments that result from each 4 vertex combination. In the end, all these segments together will form the object's contour. A simple example of this process is shown in figure 4.7.

To transition from two to three dimensions it is just a matter of employing cubes instead of squares. Although each cube has 8 vertices, for a total of $2^8 = 256$ possible combinations of how the surface might cross the cube, only 15 are geometrically different, with the rest being rotations of these, figure 4.8.

The final result of this algorithm is then saved as an *.stl* file that can be used to 3d print the models.

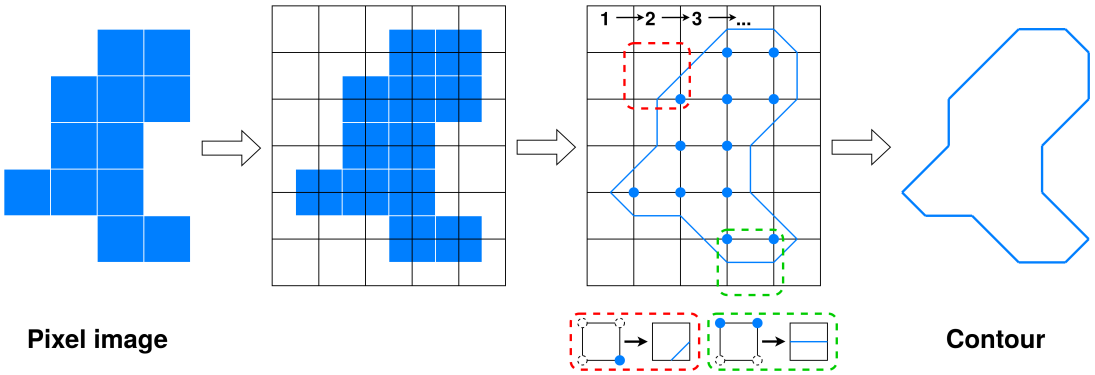


Figure 4.7: Marching squares diagram. We begin by placing a grid on top of the original image. This grid's vertices are placed in the center of the existing pixels and a value is attributed to them depending on weather they belong to the image or not. Each square of this new grid is then evaluated and a contour section placed depending on the combination of pixels found. Above, the squares are numbered in the order in which they would be analyzed and in red and green two examples of how the vertex combinations are matched to a contour segment were highlighted.

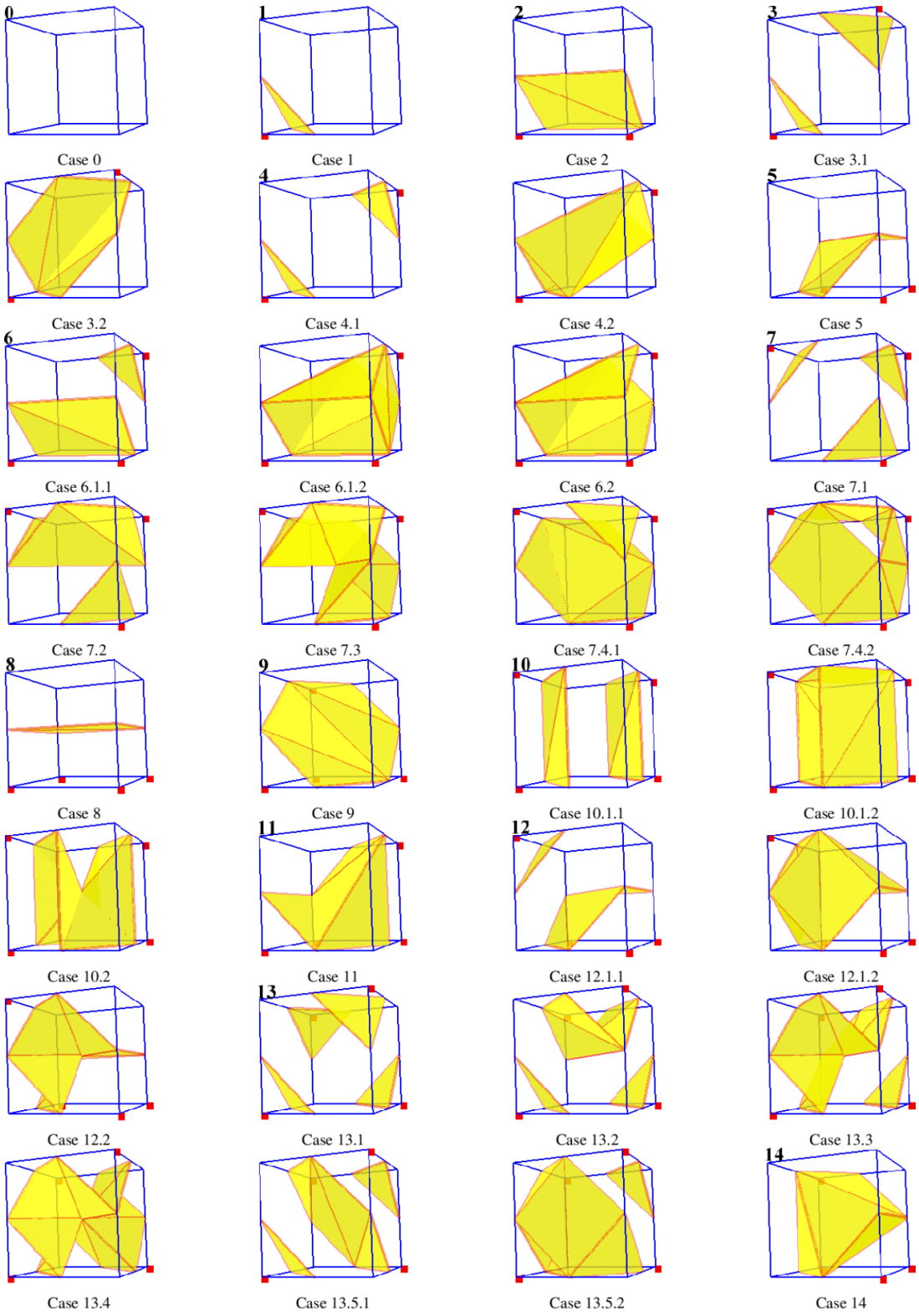


Figure 4.8: Lookup table for the marching cubes algorithm. It is obvious that there are more than 15 cubes depicted but that is due to some vertex combinations having multiple possible solutions for the surface that cross it.

# Chapter 5

# Materials and Methods

This chapter will be divided into three parts. We will begin by going through the image processing steps, followed by the creation of the material used for the final step of 3d printing the models on the final part.

## 5.1 Image processing

For processing the medical images that resulted in the head models a computer with the Linux operating system Ubuntu 18.04.2 LTS was used along with Python 3.6.8 with the modules: natsort, pydicom, nibabel, numpy, matplotlib, SimpleITK, scikit-image, ipyvolume and scipy.

The dataset used for the cranium segmentation was obtained on the cancer imaging archive website [28]. This dataset was taken from the collection Head-Neck Cetuximab, patient 0522c0027 taken on May 17th 2000. The data-set for brain segmentation features a GR (gradient recalled) sequence. In table 5.1 we can find a summary of each data set's information and, in figure 5.1, three slices of each dataset: one for each anatomical plane.

Table 5.1: Dataset summary table

| Data-sets | Resolution [$mm$] | Size [$px$] |
|---|---|---|
| CT | (696, 512, 512) | (3.0, 1.171875, 1.171875) |
| MRI | (1.0, 0.9766, 0.9766) | (186, 256, 256) |

This section has been divided into four parts: segmenting CT and MRI images in to generate the main brain structures' models and designing the cranium and brain phantoms. The most important python module used was SimpleITK, containing all the image processing functions.

### 5.1.1 Cranium segmentation

The first step was loading the CT data set using the pydicom module. The full data set contained a full body scan so it was cropped just bellow the upper jaw and its intensities rescaled from 16 to 8 bit to reduce their size and improve the processing speed. Afterwards a median filter of radius 2 was applied to improve the following segmentation steps' results. A threshold filter with a lower intensity threshold of 80 was applied for a rough segmentation before using a confidence connected filter. Finally, to close some small holes, a morphological close image filter was applied and the cranium model saved.

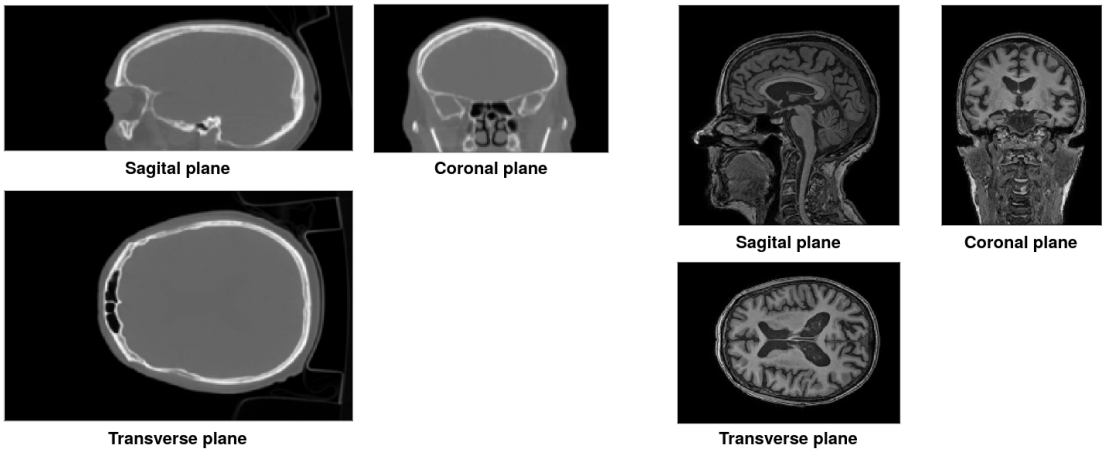


(a) CT data-set (b) MRI data-set

Figure 5.1: On the left we can see three slices of the CT scan from which we will be trying to segment the cranium, corresponding to the bright white structure. On the right we can find the MRI dataset with many irrelevant tissues for the task at hand that will be removed in the pre-processing phase using the techniques mentioned in the previous chapter.

Table 5.2: Cranium segmentation parameters

| Median | Threshold | Confidence connected | Morphological close |
|---|---|---|---|
| Radius: 2 | Lower limit: 80 | Seeds: [55,125,30] | Radius: 2 |
| — | Upper limit: 255 | Num. of iterations: 10 | Kernel type: Ball |
| — | Outside value: 0 | Multiplier: 2,5 | — |
| — | — | Init. neighborhood rad.: 2 | — |

### 5.1.2 Brain segmentation

The first thing we did to the MRI images was filtering the bias field, using the N4ITK bias fileld correction filter [22]. The before, after and the bias field itself can be found in figure 4.1. We then proceeded to remove all non-brain matter present in the images: using the BET tool [23] we extracted a binary mask of the brain that we applied to the volume. By looking at the resulting image we can see that some parts of the brain are removed so that a binary dilate of radius 1 was applied to the mask. In figure 5.2 we present a direct comparison between “before” and “after” dilating the brain mask. To finish the pre-processing phase we applied a median filter of radius 1 to remove some noise that may still be present.

We now have the base volume from which we will extract the ventricles, white and grey matter.

Table 5.3: Brain pre-processing parameters

| BET | Binary dilate | Median |
|---|---|---|
| -R | Radius: 1 | Radius: 1 |
| -f 0.3 | Kernel type: Ball | — |
| -g 0 | — | — |
| -n | — | — |
| -m | — | — |

The ventricles are a hollow structure filled with cerebrospinal fuid (CSF) which is what we will actually be segmenting. Because the CSF isn’t all concentrated in the brain ventricles, the first time we

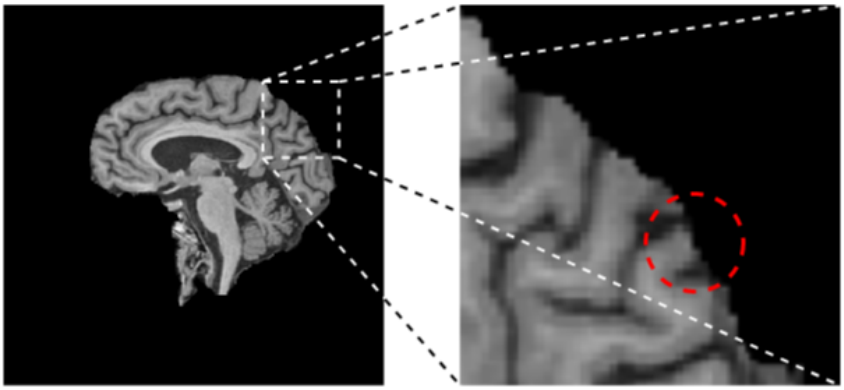

(a) Before

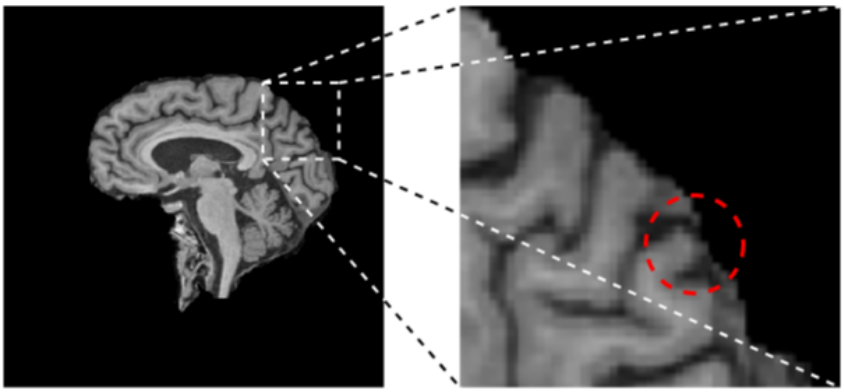

(b) After

Figure 5.2: Before and after dilating the brain mask. Notice the structure in the red circle that, after dilating, we have expanded the structure to its natural border instead of the one dictated by the BET tool.

apply the region growing algorithm we will obtain a region with a lot more than just the ventricles, shown in figure 5.3a. To extract the ventricles, we applied an image opening filter to clear any connections between the ventricles and the rest of the CSF and re-run the region growing algorithm, along with an image closing filter to eliminate any small holes left, figure 5.3b. A summary of the functions used and its parameters can be found in table 5.4

Table 5.4: CSF segmentation parameters

| Confidence connected | Open | Confidence connected | Close |
|---|---|---|---|
| Seeds: [118,96,93] | Radius: 2 | Seeds: [155,105,72], [130,91,76], [122,91,100] | Radius: 1 |
| Num. of iterations: 1 | Kernel type: Ball | Num. of iterations: 1 | Kernel type: Ball |
| Multiplier: 2.5 | — | Multiplier: 2.5 | — |
| Init. neighborhood rad.: 1 | — | Init. neighborhood rad.: 1 | — |

To segment the white and grey matter we will employ a similar procedure. We select seeds for each structure and execute the region growing algorithm. This time the tissues we are segmenting represent only their respective structures so that there is no need for any correction steps. After some iterative alterations we decided to use the parameters shown in table 5.5.

We can now proceed to designing the phantom based on the models we just segmented.

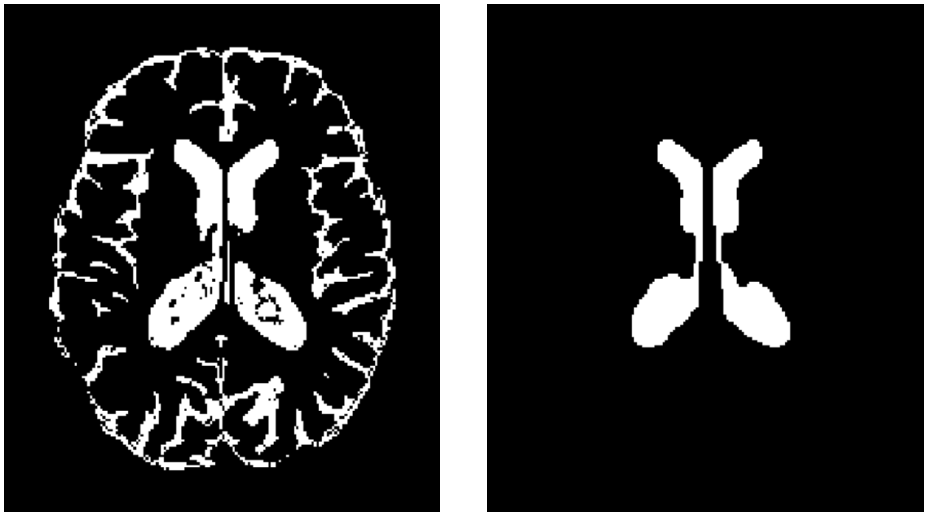

(a) (b)

Figure 5.3: In figure a) we can see the results of the first time we applied the segmentation algorithm to the CSF. As we can see it shows the distribution of CSF in the entire brain. On figure b) we have the results after we eliminated the connections between the ventricles and the rest of the CSF regions, re-run the algorithm, and manually corrected some wholes that still existed.

Table 5.5: WM and GM segmentation parameters

| White matter | | Grey matter | |
|---|---|---|---|
| Confidence connected | Closing | Confidence connected | Closing |
| Seeds: [88,93,109], [160,148,109], [176,87,69] | Radius:1 | Seeds: [106,63,106], [102,70,68] | Radius:1 |
| Num. of iterations:1 | Kernel type:Ball | Num. of iterations:1 | Kernel type:Ball |
| Multiplier:2.5 | — | Multiplier:2.5 | — |
| Init. neighborhood rad.:1 | — | Init. neighborhood rad.:1 | — |

### 5.1.3 Cranium phantom design

There are two problems in the cranium model hat we must correct: For reasons we will be reviewing in section 6.1.1 the cranium model is thicker than it should and because it comes from from a different dataset than that of the brain, they sizes do not match.

The cranium model is in fact smaller than it should and the brain model does not fit inside it. The first step is to scale up the model. This re-scaling results in an increased cranium thickness that, as mentioned above, would have to be corrected for anyways.

The final step is to remove the excess cranium material utilizing a dilated model of the grey matter.

Both the re-scaling of the cranium and location of the grey matter inside it were manually selected.

After this we convert the volume to a surface using the marching cubes algorithm, saving it to a *.stl* file. The results are shown in figure 6.2a.

The model is too large to be printed in one single piece so we had to split it into multiple pieces with maximum dimensions of $10 \times 10 \times 5cm$. We used blender to for this operation and in the end divided it in halves, thirds and fifths with the sagital, coronal and transverse planes, respectively, resulting in a total of thirty pieces.

### 5.1.4 Brain phantom design

For the brain the process is not as straight forward. We must take the organ models' we wish to build a phantom for and obtain the walls that will contain the radiotracer representing them.

The grey and white matter can be represented by either separate chambers, or a continuous one with different porosities for each tissue. To simplify things, for now, we will only try to model the grey matter chamber.

We obtain the outer walls by taking the grey matter model and applying a closing filter of radius 5 to it followed by SITK's *BinaryContourImageFilter*. This wall is too thin to be printed so the last step is to dilate it with a ball kernel of radius 1.

For the inner wall we begin by closing the white matter model with a kernel of radius 2. To be certain that there is empty space between the inner and outer walls, the latter are dilated with a kernel of radius 3 and subtracted from the former using logical operations.

Table 5.6: Parameters for obtaining the brain phantom walls

| Inner wall | | Outer wall | | |
|---|---|---|---|---|
| Close | Dilate | Close | Contour | Dilate |
| Radius: 2 | Radius: 3 | Radius: 5 | SetBackground: 0 | Radius: 1 |
| Kernel type: Ball | — | Kernel type: Ball | SetForeground: 0 | — |

In the end both models were merged into one, converted from voxels to a surface and exported as a *.stl* file that we opened with blender to examine and correct any errors like floating artifacts that were found.

## 5.2 3d print preparation

### 5.2.1 Mixure composition

Bones are up to 70% in weight of hydroxyapatite (HA) and as such it seems like a good central component of a bone equivalent mixture. To hold it together we'll use Polycaprolactone (PCL). These are the 2 components of the mixture we'll be making but before doing it we must decide on the actual proportions of these 2.

We begin by looking at the mass attenuation coefficients of water and cortical bone, table 5.7, with which we're going to calculate the bone's Hounsfield units using equation 2.4 and $(\mu/\rho)_{air} \approx \mu_{air} \approx 0$.

Table 5.7: Mass attenuation coefficients of water (a) and bone (b). Taken from [29]

| Water (liquid) | |
|---|---|
| Energy $[KeV]$ | $\mu/\rho[cm^2/g]$ |
| 50 | 0.2269 |
| 100 | 0.1707 |
| 200 | 0.1370 |
| $\rho = 1g/cm^3$ | |

(a)

| Cortical bone | | |
|---|---|---|
| Energy $[KeV]$ | $\mu/\rho[cm^2/g]$ | HU |
| 50 | 0.4242 | 2458 |
| 100 | 0.1855 | 1010 |
| 200 | 0.1309 | 767 |
| $\rho = 1.85g/cm^3$ | | |

(b)

Then, based on the mass attenuation of PCL and HA, table 5.8, we can employ equations 2.3 and 2.4 to calculate the properties of PCL/HA mixtures with ratios 70/30, 60/40 and 50/50.

Table 5.8: Mass attenuation coefficients of PCL (a) and HA (b).

| PCL, $C_6H_{10}O_2$ | |
|---|---|
| Energy $[KeV]$ | $\mu/\rho[cm^2/g]$ |
| 50 | 0.2075 |
| 100 | 0.1650 |
| 200 | 0.1337 |
| $\rho = 1.145 g/cm^3$ | |

(a)

| HA, $Ca_5(PO_4)_5OH$ | |
|---|---|
| Energy $[KeV]$ | $\mu/\rho[cm^2/g]$ |
| 50 | 0.5867 |
| 100 | 0.0.2019 |
| 200 | 0.1297 |
| $\rho = 3.18 g/cm^3$ | |

(b)

The results are graphed in figures 6.12 and 6.11. The 70/30 mixture was tested using a micro CT system but the results obtained are had many mistakes that led to them being inconclusive so they will not be included.

### 5.2.2 Blending the mixture components

We can employ 2 methods to blend the 2 components: melt blending and solvent casting. Melt blending doesn't guarantee a mix as homogeneous as solvent casting but provides it faster. This method was used to mix 3 small batches of 30 g of 70/30, 60/40 and 50/50 mixtures to test with the micro CT before making the bigger batch used for the cranium pieces. We start by measuring the adequate quantities of PCL pellets and HA powder* for each mix and heating the PCL at 100 °C for 40 min. After this period we increase the temperature to 150 °C and once the PCL has melted completely we start progressively adding HA powder while mixing. When all the HA has been mixed all that is left is making small pellets and letting them cool.

Solvent casting, by using a solvent, guarantees a better mix of the HA in te PCL, at the cost of the extra time that we must allow for its evaporation. This method was used to mix 250 g of the 50/50 mixture that will be used to print the a cranium piece. The first step in this method is dissolving the PCL pellets in dimethylformamide (DMF) with a ratio of 2 mL for every 0.5 g of PCL. Then, we set the magnetic stirrer to 500rpm and start gradually dissolving the HA powder. Once all the HA has been dissolved we place it in several petri dishes and leave it to dry. After around 5 days it was ready and we cut the PLC/HA discs into small pieces for storage.

## 5.3 BioMaTe 3d printer

Now that we have the models and the material with which to print them we can move on to the final steps. Before sending the models to the printer we must 1st slice them, ie, go from an *.stl* file to g-code that the printer can understand. First we'll go over the CAMOS (computer aided manufacturing of scaffolds) software used for this and then move on to the actual 3d printing process and how to operate the Biomat 3d printer.

### 5.3.1 Slicing the models

To turn the *.stl* files into G-code we used the CAMOS software developed at CDRSPs. The "transform settings" are used to scale and rotate the model and were all left at their default settings. The nozzle installed on the 3d printer had a diameter of $0.3mm$ so that was the fill distance (the space between each

*5 µm HA particles

line) used in order to leave no pores in the final piece. To make sure the individual layers would cohere the distance between slices was set to slightly less. Regarding the number of layers and lines we only need to make sure that they are enough for the path to cover the entire piece. Each layer is oriented 90°in relation to the previous so that the angles are set to $[0,90]$, 0 corresponding to the even numbered layers and 90 to the uneven. An overview of the CAMOS GUI can be found in figure 5.4 and a brief summary of all the settings used in table 5.9.

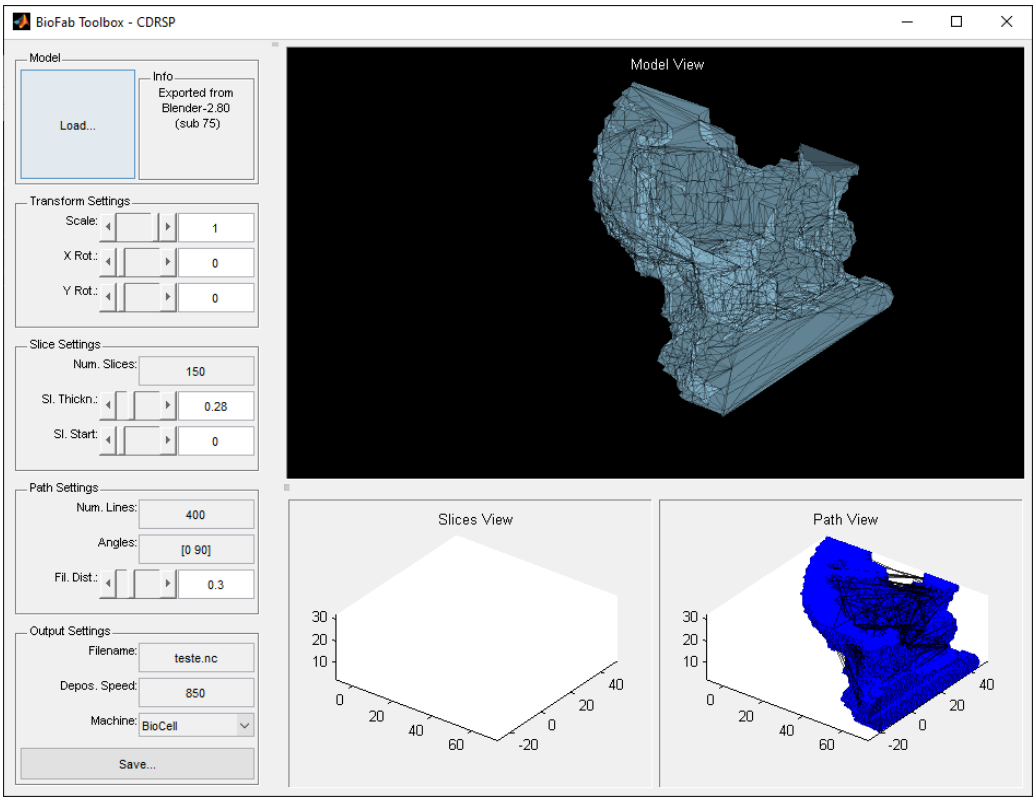


Figure 5.4: CAMOS software GUI. We can see the 3 main visualization: on the left we can areas. To run this software we must have Matlab Compiler Runtime (MCR) version 7.13 installed.

Table 5.9: List of settings used to slice the models using the CAMOS software.

| Transform settings | | Slice settings | | Path settings | | Extrusion speed |
|---|---|---|---|---|---|---|
| scale | 1 | num. slices | 125 | num. lines | 450 | $850mm/min$ |
| x rot. | 0 | sl. thickness | $0.28mm$ | fill dist. | $0.3mm$ | — |
| y rot. | 0 | — | — | angles | [0,90]° | — |

The output comes in the form of a text file that we must edit before proceeding. Its header is missing some lines that setup the printer's extrusion velocity and starting position as well as the final STOP commands. Editing these is just a matter of opening the file with a text editor and manually introducing the commands.

We now have the necessary files and can proceed to the final step of printing the parts, as described in the next subsection.

### 5.3.2 3d printing

We can now proceed to finally printing a piece of the skull. We used a nozzle with a diameter of $0.3mm$ and the temperatures of the extruder, deposit and "L" arm were set to 93, 140 and 140°C, respectively. It was during this time that various extrusion speeds were tested, paired with various extruder temperatures, until we settled on an extrusion speed of $850mm/min$. On chapter 6.3 we discuss the iterative process that resulted in these parameters.

This 3d printer doesn't have a heated base so in order to control the printing environment and minimize any changes to the related variables, especially surrounding temperature, a heat gun, set to 60°C was placed inside the machine along with a thermocouple to monitor it. By maintaining a higher temperature we hoped to increase the cohesion between layers and reduce the overall warp associated with larger 3d prints.

The tank isn't big enough for us to leave it continually printing over its full duration. As such this part was printed over 2 work days with pauses for refill approximately every 2-3 hours. On the second day the already print piece was heated up with the heat gun before continuing so that the new layers would adhere better.

Once it was done all excess material was removed using pliers and a scalpel.

# Chapter 6

# Results and Discussion

We will now present the results of the methodology present in the last chapter. This chapter will have the same structure as the previous one: we will begin by looking into the image segmentation results, followed by the phantom design and ending with the printing process of the phantom.

## 6.1 Segmentation

### 6.1.1 Cranium

In figure 6.1a we have the initial CT data-set, for reference, with the skull segmentation results on its right, figure 6.1b. The outer contour of the skull was successfully segmented, unfortunately, as we can see by comparing the model with the original CT images, the skull as a whole is much thicker than it should. This happened because, as we can see in figure 6.1a there are some places in the dataset where bone intensity decreases (notice the eye socket area) that forces us to allow for a greater interval of the pixel intensities that will belong to the cranium model (larger c value in section 4.2.2). Afterwards we ended up having to scale up the cranium model which added more excess material that was then carved out using the segmented brain model. This was one of the reasons we scaled up the skull model instead of scaling down the brain one. We would always have to carve out the excess skull and this way we would only be manually altering one of the models.

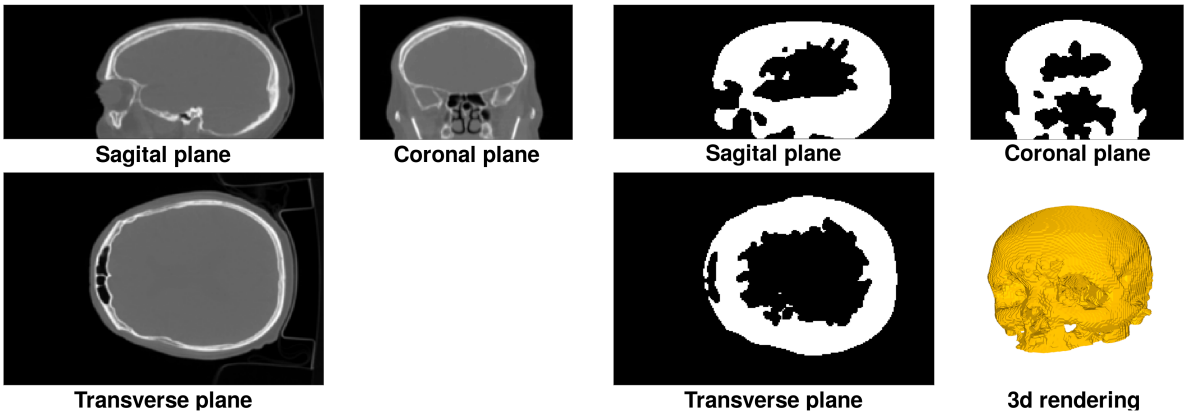


(a) CT data-set (b) Skull model

Figure 6.1: Side-by-side comparison of the final model with its original dataset. The three slices correspond to the voxelized image while the 3d render corresponds the surface obtained from it.

There were also some stair casing effects, related to the shift from a voxelized model to a surface, using the marching cubes algorithm. Since we obtained these surfaces from a voxelized image, although we weren't expecting these artifacts, it makes sense that they exist. The surface models are presented in figure 6.2a where we can see these artifacts. When separating the model into multiple pieces, one of the effects of decimating some of the surface geometry is the mitigation, albeit reduced, of this effect, figure 6.2b. In the final 3d printed piece we did not find any evidence of these artifacts even though we did not try to smooth them out by any additional means.

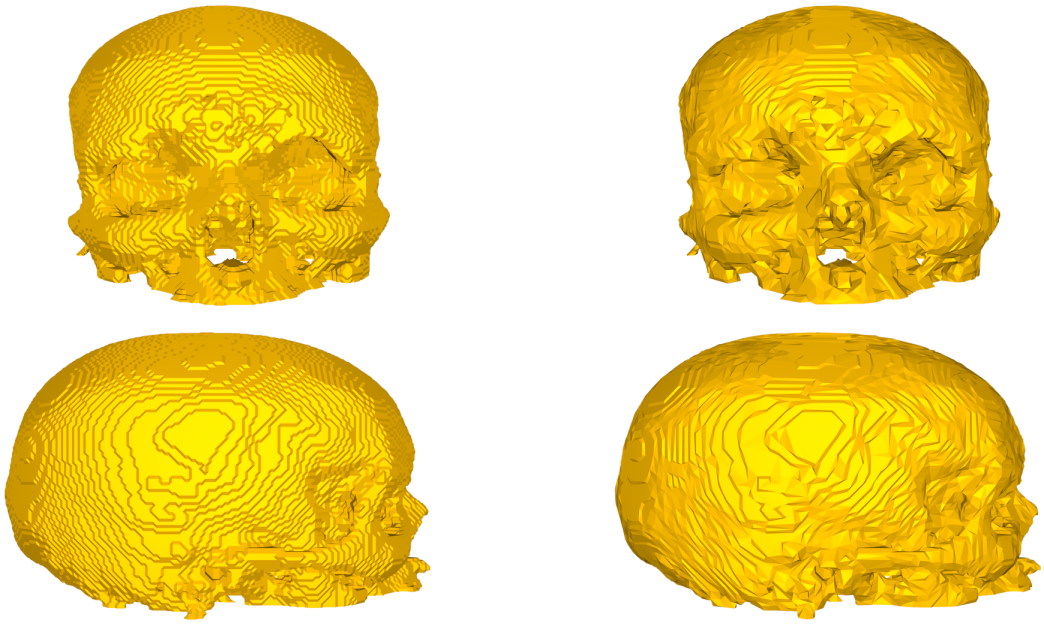

(a) (b)

Figure 6.2: On the left we show the results of the marching cubes algorithm. The surface on the right was obtained in blender by eliminating 85% of the polygons that formed it.

When dividing the skull model in sizable pieces for the 3d printer many floating structures were found inside it. We have no good explanation for their exitence for since we used a region growing segmentation method and these artifacts are loose inside. They are in the are that was removed using one of the brain models so they might have been caried from that model to this one but we do not know for sure. One of these artifacts is shown in figure 6.3.

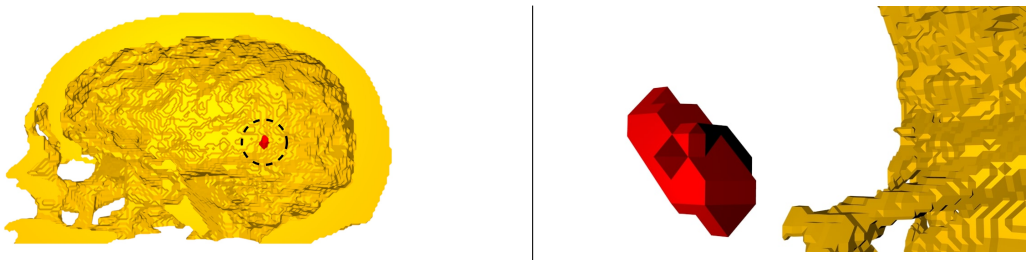

(a) (b)

Figure 6.3: In this image we present one of the floating artifacts we found after cutting the model in half. This piece was manually removed.

### 6.1.2 Brain

For the brain, just like for the cranium, we will begin by showing a side-by-side comparison of the original dataset with the three segmented structures (grey matter, white matter and ventricles) in figure 6.4.

We will first review the ventricles segmentation, followed by the grey and white matter, in that order.

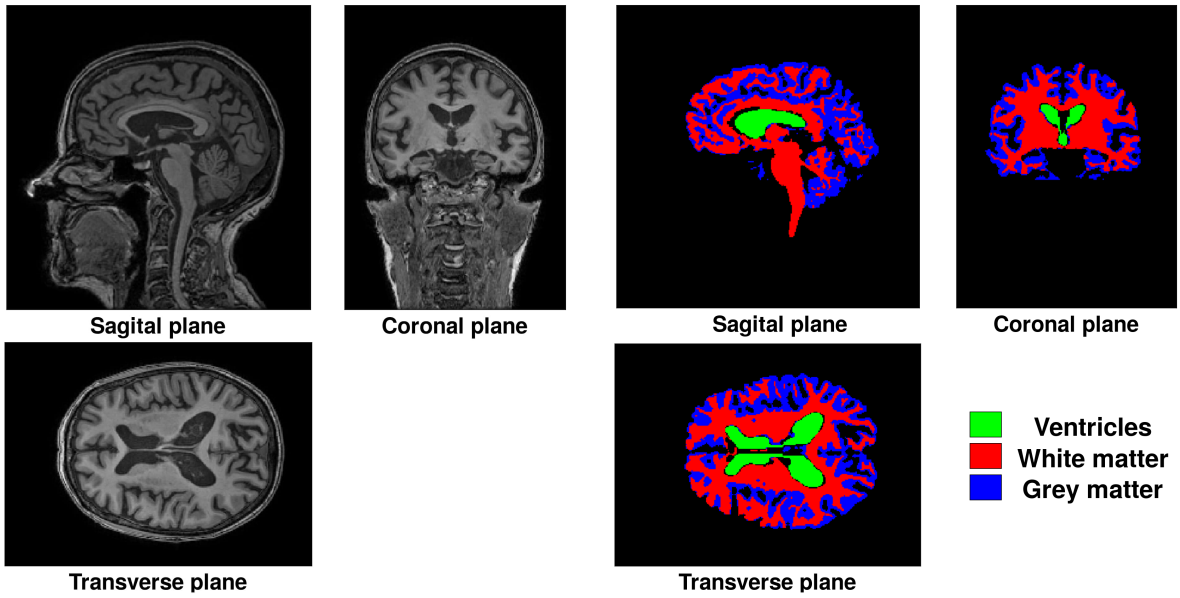


(a) MRI data-set (b) Brain segmentation results

Figure 6.4: Side-by-side comparison of the final model with its original dataset.

#### Ventricles

We have achieved an overall good ventricle segmentation as we can see in figure 6.5 where we can see the main shapes of the lateral and third ventricles. If we look at an image of the sagital plane, figure 6.6a, we can see a gap in the white matter where the ventricles haven't been segmented. While trying to close some of the bigger holes in the model right after applying the region algorithm, unfortunately, the space in the middle of the ventricles ended up being filled out. The manual attempts at clearing it resulted in the unnatural borders we can see in figure 6.6b.

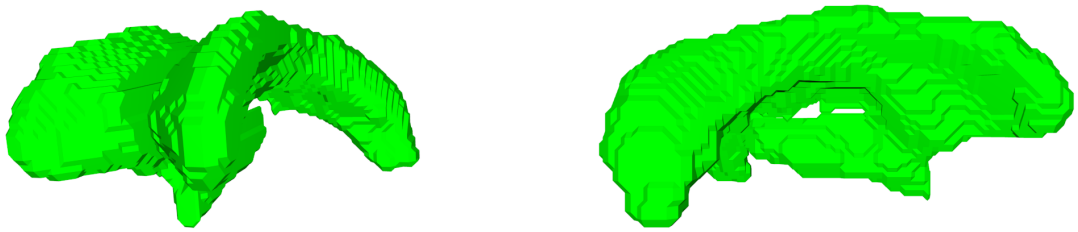

(a) (b)

Figure 6.5: Rendering of the ventricle models. Just like with the skul model some stair casing effects can be seen

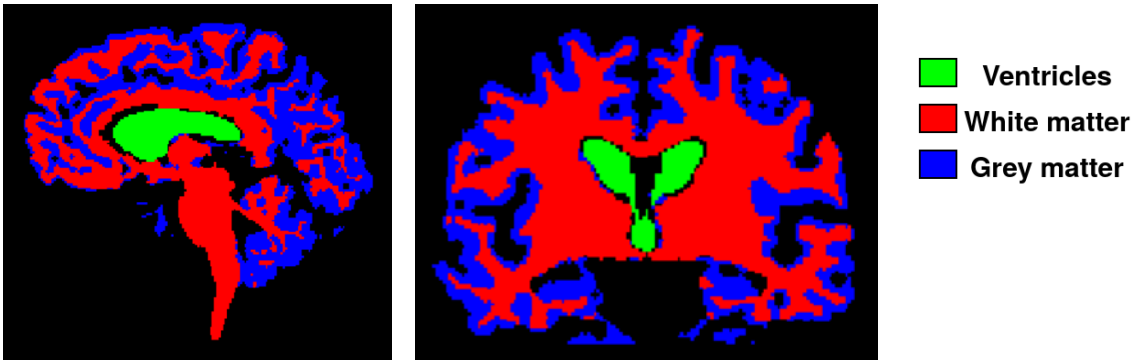


(a) (b)

Figure 6.6: In this figure we show two anatomical planes of the segmented models. On the left we can see where some of the ventricles were not segmented, mainly towards the posterior region where they should have curved downwards. On the right we can see the sharp edges in between the lateral ventricles.

### Grey and white matter

Regarding the grey and white matter segmentation, we present in figure 6.7 two planes with both results overlaid.

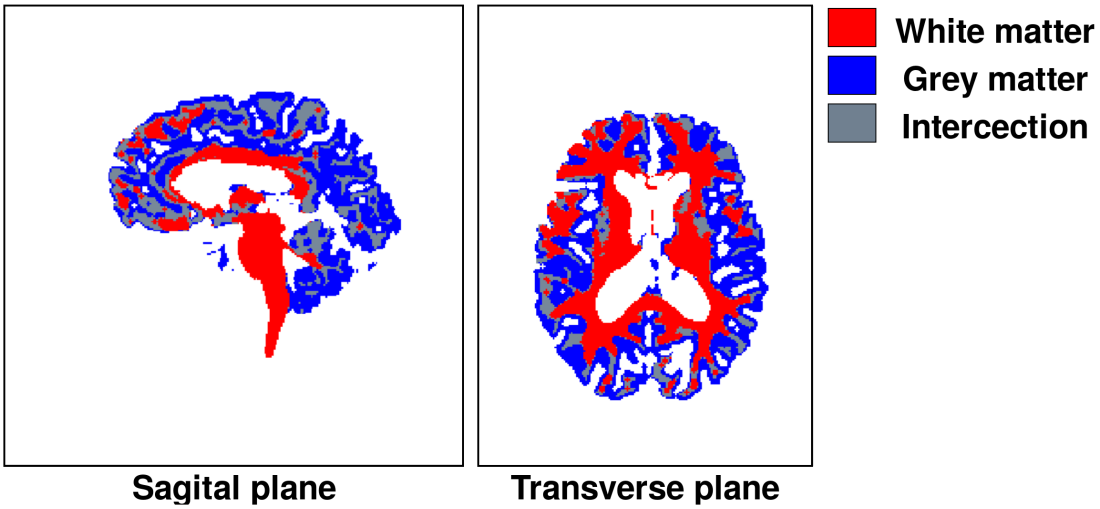


Figure 6.7: In this figure we present two anatomical planes of both grey and white matter segmentation along with the regions in which they intercept with each other.

The first thing we can notice is that there is a substancial overlay of the two models, which makes sense, given that if we inspect the original images we can see that the difference in intensities between grey and white matter is subtle.

In the end we have defined the intersections as white matter. There were two reasons for this choice: We can think of the brain as a grey matter layer enveloping the white mater that provides its structure. By doing this we can more accurately obtain the shape of the grey matter based on the white matter than if we had defined the intersections as grey matter. Also, if we had done the opposite we would be losing a lot of the white matter model while maintaining some spots that are not enveloped in grey matter. This way we move the errors we are inducing from the segmentation we are more confident in to the one we already know contains some errors. In figure 6.8, we show a 3d render of these models.

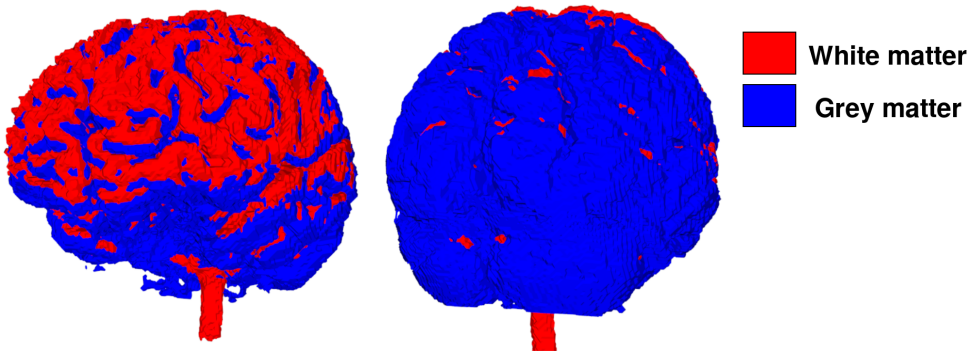


(a) (b)

Figure 6.8: Render of the grey and white matter models from the front, (a), and back, (b).

## 6.2 Phantom design

### 6.2.1 Model

Our objective was to have a hollow space representing grey matter. In figure 6.9 we show the the results we obtained based on the segmented models of the grey and white matter.

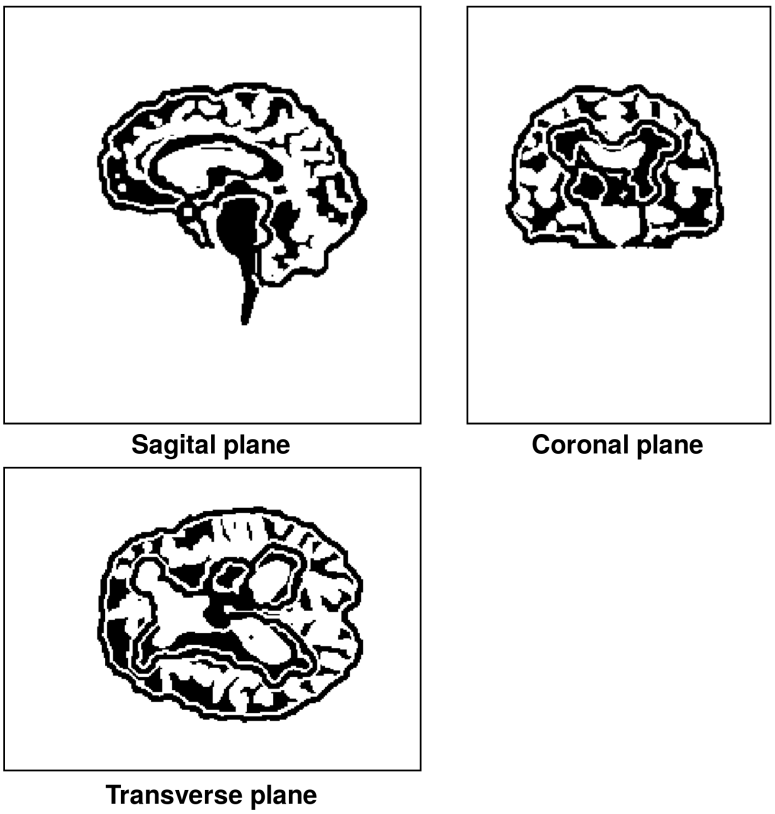


Figure 6.9: In this figure we can see three cutouts of the brain phantom model, one across each anatomical plane. Black represents the walls that would be printed.

Since we were trying to create an empty compartment corresponding to the grey matter, the phantom and brain models should have a one-on-one mapping between the grey matter and the empty spaces. In figure 6.10 we show a side-by-side comparison between both models.

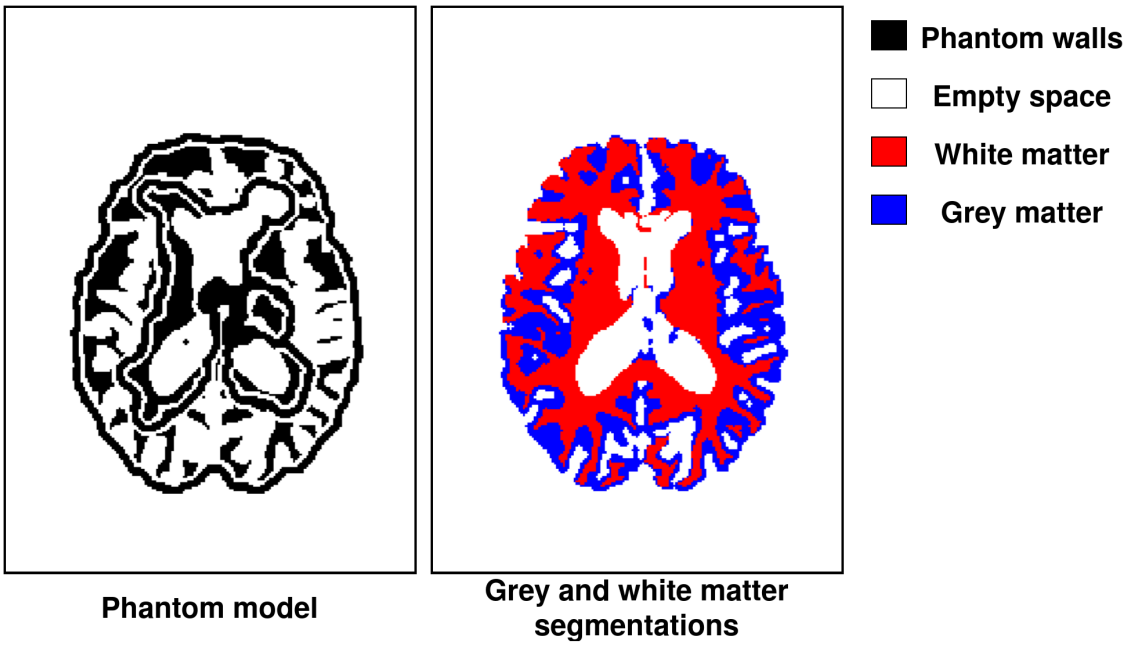


Figure 6.10: Side-by-side comparison of the brain phantom generated based on the segmented models of grey and white matter.

As we can see, there are several differences between the white empty spaces and the blue region corresponding to the grey matter. The one that stands out the most is the continuous (thin) cavity that surrounds the model while we can clearly see that in some of those areas no grey matter has been segmented (as previously mentioned).

Some confusion may arise from the ventricles also appearing as being hollow in this model. This happens because the grey and white matter models themselves, used in the design phase (section 5.1.4), dare hollow in this region. Which makes sense, because that region should contain the ventricles then it will not contain neither grey nor white matter. Since there is a wall around this structure even though it is hollow, it is a distinct cavity from the grey matter one.

When inspecting the model for the viability of 3d printing it, we find that it would need a lot of support material that would be very difficult, if not impossible, to remove due to its interior structures that would be too close together.

In the end, the biggest errors are still more related to the shape of our target organs and while we should not forget about the practical necessities of the model, for now, we should try and improve the overall shape of the phantom. While for this, better segmented images are always best, the problems arise ore from how we utilized them to build the phantom.

### 6.2.2 Phantom material

We will now review the materials with which we will print the phantom. Since the brain phantom did not have enough quality to print it we will focus only on the materials used to 3d print the cranium model. More so, for the brain phantom the material composition is not as important as the shape it will hold, since the properties we will be measured will arise not from the material itself, but from the radiotracer

within.

### Composition

The calculated mass attenuation coefficients and Hounsfield units for the different mixture ratios are presented in figures 6.11 and 6.12.

If we only look at the mass attenuation coefficients we are pulled towards the conclusion that we need a higher still ratio of HA to PCL. These values however do not take into account the different densities of each material (see table 6.1). Cortical bone density (table 5.7b) lies between that of the 70/30 and 60/40 mixtures so its Hounsfield units value is smaller than our 50/50 mixture.

Our custom material also behaves differently from bone throughout the energy specter so that it will only mimic it for a narrow band, which we might choose to better suit our needs.

We're expecting the 3d printed objects to have lower Hounsfield units than these due to some pores and lower material densities in the final pieces that may occur during the 3d printing process so we will make the 50/50 mixture to 3d print the final objects.

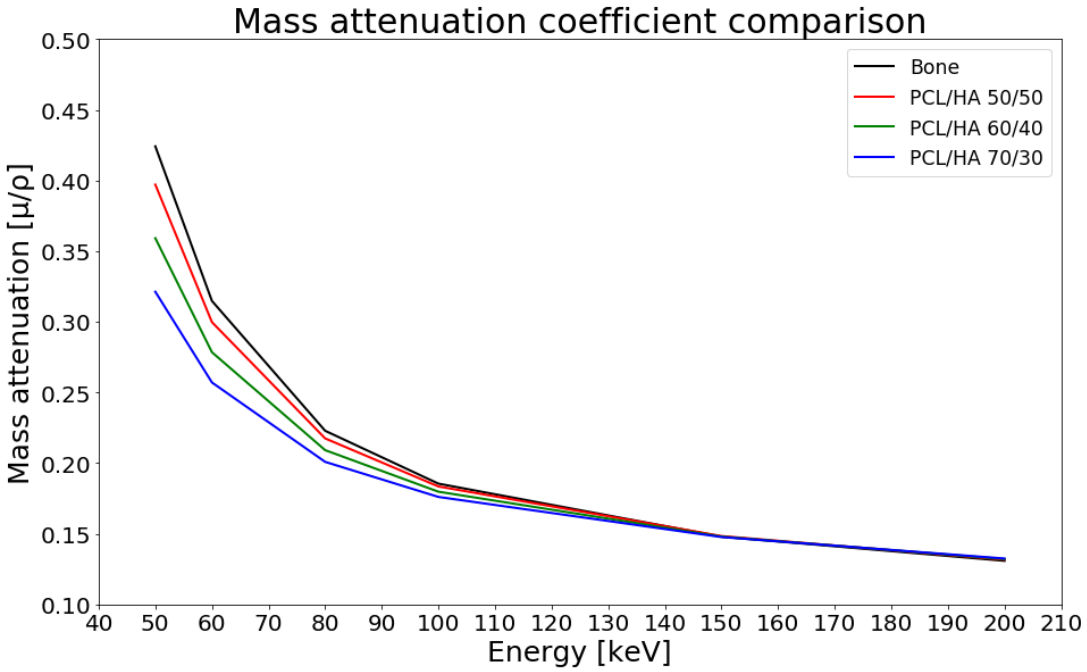


Figure 6.11: Comparison of the theoretical mass attenuation coefficients of each PCL/HA ratio to cortical bone. The most relevant energies are those around 120Kev, since they are the ones usually used in CT.

Table 6.1: Density of the various PLC/HA ratio mixtures

| Ratio (mass) | Density $[g/cm^3]$ |
|---|---|
| 50/50 | 2.1625 |
| 60/40 | 1.9590 |
| 70/30 | 1.7555 |

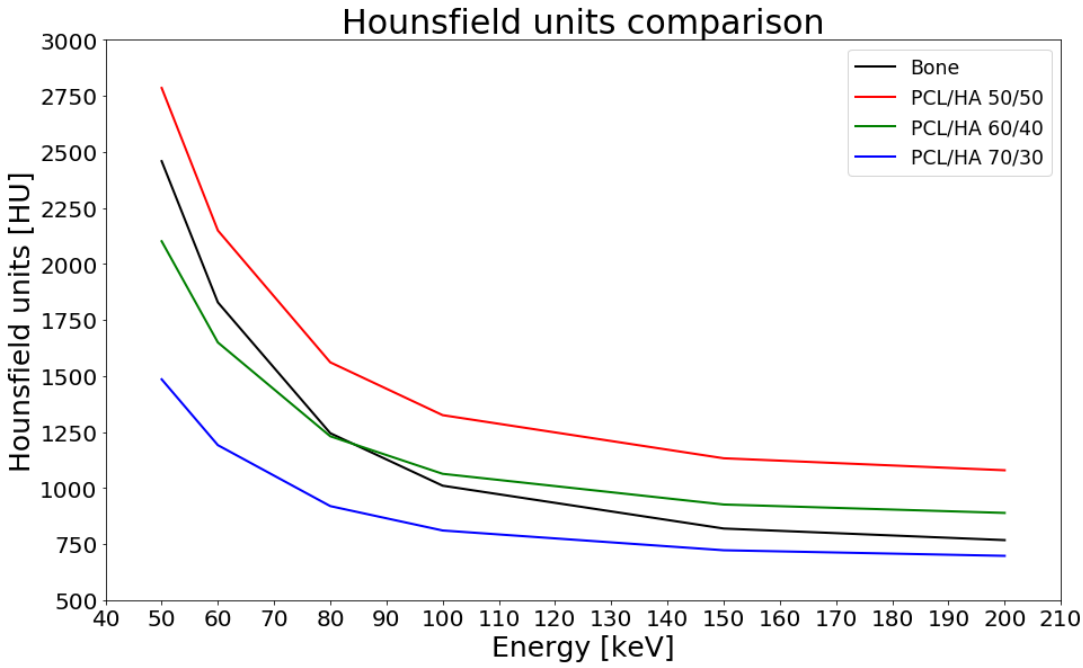


Figure 6.12: Comparison of the Hounsfield units of each material across the energy spectrum. Because to calculate the hounsfield units we had to take into account the densities os each material this will provides a better intuition of how the materials will behave in real world tests.

### Mixing method

With melt blending we get smooth pellets, as large or small as we make them (see figure 6.13a) while solvent casting results in something akin to shredded tissue stripes (see figure 6.13b).

(a) Melt blending

(b) Solvent casting

Figure 6.13: On the left we can see the pellets that result from the melt blending process. On the right we show the solvent casting results, corresponding to stripes of material that were cut from round pieces the size of a petri dish.

We did not employ both methods at the same time and unfortunately did not manage to perform any quantitative tests so that their comparison will be a merely qualitative one. Melt blending is the simplest method, but also the most prone to a less homogeneous final result since it demands more effort to effectively mix the materials while the solvent casting method, by utilizing a solvent alleviates a lot of the effort while ensuring a better mix of the components. Both methods require the same amount of

time to prepare (minus the waiting period for the solvent casting where we just wait for the solvent to evaporate) with the main disadvantage of the solvent casting being the wait period of around five days for the solvent to dry out versus the immediate availability of the melt blending mixture.

## 6.3 3d printing

We will now proceed to discuss the results of the 3d printing process, firstly describing the parameter tuning phase and, afterwards, reviewing the final print piece.

### 6.3.1 Parameter tuning

This was above all iterative process, where every variable, in one way or another would affect all others. Nevertheless we will separate them to ease the discussion of each individual parameter and its impact on the final piece.

#### Extrusion speed and porosity

The final result should be a solid piece without pores between its extrusion lines. To achieve this, the extrusion speed must be high enough to fill the current path that is being swept. We began with lower speeds of around $800mm/min$ but, as we can see in figure 6.14a, lots of striations were being left behind so we ended up testing several others, up to $900mm/min$, having ended up utilizing the $850mm/min$ mentioned before. To improve the material deposition we could also increase the extruder temperature which would make the material more fluid, resulting in a greater flow.

#### Layer height and cohesion

Also required to printing a solid piece is that each new layers adheres to the previous one. In early attempts sometimes the height between each layer was set too high leading to layers that could easily torn apart, as shown in figure 6.14b. It is worth mentioning that both extrusion speed and temperature also play a role in layer cohesion. The material must be deposited fast enough as to press it against the previous layer while its still hot enough to bond with it.

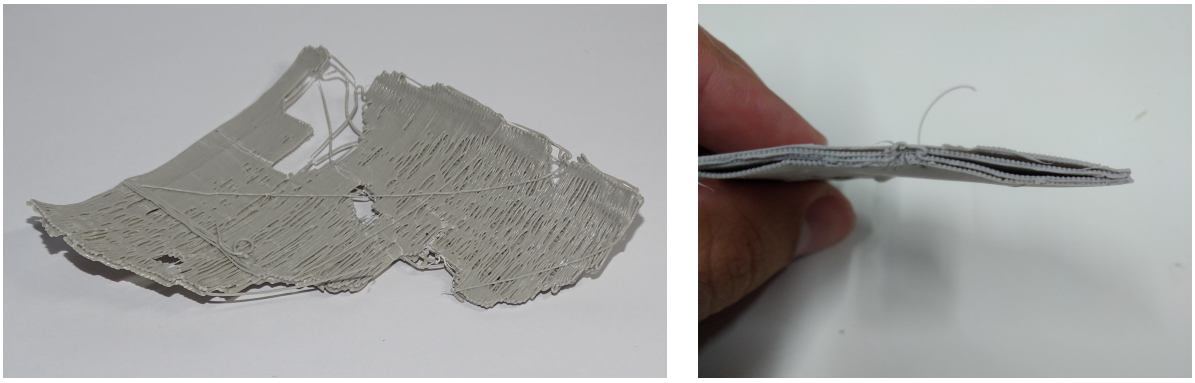

(a) Insufficient material extrusion (b) Poor layer cohesion

Figure 6.14: Early 3d printed parts. The part on the left shows many striations, derived from a low extrusion speed. On the right we show a piece whose layers did not fuse together.

**Temperature and warping effects**

Temperature influences extrusion speed and layer cohesion, both positively. Despite the obvious impulse to just increase temperature height, it can also be too high, making the material too fluid leading to the loss of some details, like we can see in figure 6.15a. Thus we tried keeping the temperature bellow 93°C.

Also related to temperature are the warping effects that occur due to uneven cooling of the piece, figure 6.15b. No heated base exists for this printer so that as soon as the material was deposited it started to cool down and, noticeable after the first half millimeter, the piece's edges would lift of the base plate. In our first attempt to minimize this effect we used a heat gun to initially heat the platform and then, during the printing process, pointed it at the piece. This resulted in a partially melted piece (figure 6.15a) because of the temperature of the heatgun that was too high and could not be controlled. In this image we can also note some slight scratching artifacts resulting from the nozzle scraping on the piece due to the warping of its edges.

In the end, a controllable heat gun was placed inside the printer, pointed away from the piece, to just try and control the air temperature which led to a significant decrease in the warping of the part. In the future a heated base should be constructed to further diminish these effects.

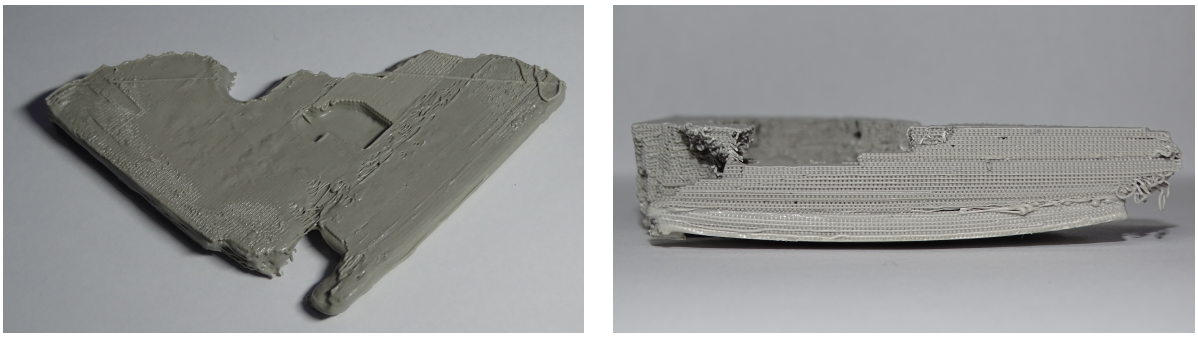

(a) (b)

Figure 6.15: Here, we show three examples of defects related to temperature control. On the left we can see that some details were lost due to partial melting of the material after extrusion, notice the rounded edges in the piece. Note also the scraping along the left diagonal, due to the warping of that side. On the right (b), the warped base is clearly noticeable on the bottom of the piece.

### 6.3.2 Final piece

In the end we managed to print one piece, over the span of two days, figure 6.16. It consists approximately of 40% of one of the thirty pieces that we would have to print in order to obtain the hole model.

Two full days to print the presented part means that to print the hole model it would be required to print for 10 hours a day for around thirty weeks (assuming 5 day weeks). The printer cannot be left printing overnight since it's deposit needed to be refilled around every two and a half hours (with the current settings). It might be possible to decrease the print time by a substantial margin by utilizing a nozzle with $1mm$ diameter since we will take only a third of the sweeps to print each layer. This will also most likely limit the pores present on the final piece by two thirds and the total number of layers. We did not try this due to the unavailability of these nozzles.

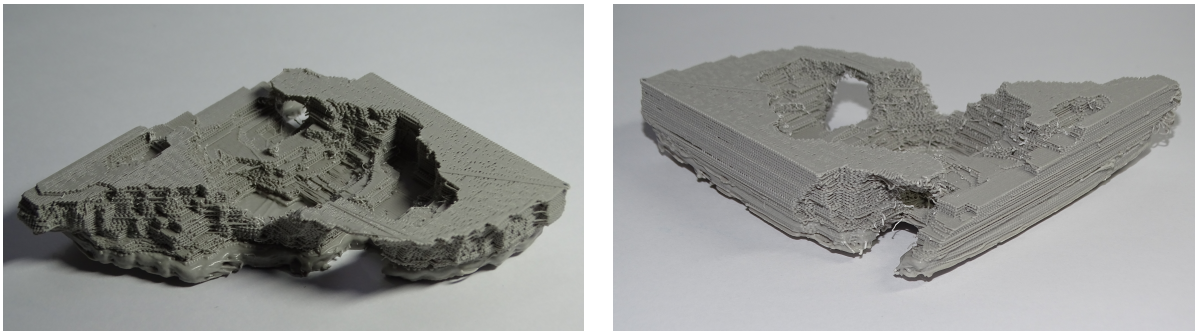

(a) (b)

Figure 6.16: Final 3d printed piece

In the places where each extends further outwards than the previous, some material falls a bit down but after some more layers this stops and the new layers will have a base on which to settle, like we can see in figure 6.16b, on the top, where an arch is formed.

Since only part of the whole model was built we cannot evaluate how accurately or not it represents the computer model. We can, however, notice that it appears to at least have the outer shape and some internal contours that should be present in the whole model.

Considering the biomate 3d printer was not designed to build pieces this large, and that no support material was used, the results show it is viable to at least print a skull phantom using the skull mimicking material. Unfortunately we were not able to test how its attenuation compares to that of real skull, which would be the final step to determine the viability of this part of the phantom.

# Chapter 7

# Conclusions and Future Work

We set out to design a realistic head phantom for PET/CT systems to, hopefully, correct for partial volume effects in brain images made with these systems.

The segmented cranium model was adequate, capturing the overall shape of the skull. We do not know the origin of the floating artifacts found inside this model. The seeded region growing method employed to segment it, however, may not be the best for the task since it is a thin structure with high variance in its intensity in CT images. In the future we should attempt to extract it from a dataset of the same patient as the brain, to reduce the manual alterations necessary for both cranium and brain models to fit together.

The brain model can be separated into three different ones: ventricles, grey matter and white matter. Just like the cranium model, we obtained a good model of the ventricles and white matter, capturing their overall shape. The grey matter model, however, did not cover the full extension of the white matter, as it should. We tried to use different seeds and parameters to improve the results but to no avail.

This failure to completely segment the grey mater is not why we failed to design the brain phantom part of our head phantom. We should have first experimented with simpler shapes, gradually modifying their shapes until we arrived at our segmented models instead of subtracting the white mater from the grey expecting a nice empty compartment, which is what we actually did. This way we can add structural supports along the way and make sure any vital constraints are met.

Once we shifted the models from voxel-based to surfaces, all presented stair-casing problems. These were partially corrected, in the skull models, when their geometries had to be simplified to allow their upload to the CAMOS software to.

Moving on to the phantom construction itself, we were only able to print one small part of the whole cranium piece. And even this with some changes made along the printing process. Even though the BIOMATE 3d printer and CAMOS software were not made with such complex structures in mind, it was possible to print a complex structure with only some minor errors. Currently, the main aspects that should be addressed are the time it takes to print, which might be massively reduced by using a larger nozzle, using a heated base plate to eliminate warping and trying to use a similar printer that may allow for support material to help print some more intricate structures without errors.

Regarding the material used to print the cranium model. One of the shortcoming os this work was the failure to test how it actually compared to the theory. There was an attempt to utilize a micro-CT machine to quantify the Hounsfied Units of an early batch but we found the results inconclusive due to many variables in the system that we could not control. One of the aspects that should be verified in the near future is the properties of this mixture of PCL/HA.

These phantoms may be used in the future to map the point spread function of a PET system, by

comparing the generated images to the segmented models. With these phantoms it might be possible to achieve better results than with the point sources used in [8].

Future improvements to the phantom can be to eventually allow for multiple chambers that communicate with each other, to create a dynamic phantom. Early work on this can be found in [30]

This work was the starting steps of a larger, more complex project, and therefore, a more simplistic approach to the design problem at hand. It provided a good look on the main problems that need to be solves and gives us clear objectives to improve on in the future.

# Bibliography


[1] European Society of Radiology (ESR et al. "Medical imaging in personalised medicine: a white paper of the research committee of the European Society of Radiology (ESR)". In: *Insights into imaging* 6.2 (2015), pp. 141–155.

[2] Abass Alavi et al. "Correction for partial volume effect is a must, not a luxury, to fully exploit the potential of quantitative PET imaging in clinical oncology". In: *Molecular Imaging and Biology* 20.1 (2018), pp. 1–3.

[3] EJ Hoffman et al. "3-D phantom to simulate cerebral blood flow and metabolic images for PET". In: *IEEE Transactions on Nuclear Science* 37.2 (1990), pp. 616–620.

[4] Thore M Bücking et al. "From medical imaging data to 3D printed anatomical models". In: *PloS one* 12.5 (2017), e0178540.

[5] P Hogg, G Testanera, et al. *Principles and practice of PET/CT: part 1: a technologists guide*. 2010.

[6] PE Kinehan and JW Fletcher. "PET/CT standardized uptake values (SUVs) in clinical practice and assessing response to therapy". In: *Semin Ultrasound CT MR* 31.6 (2010), pp. 496–505.

[7] Marine Soret, Stephen L Bacharach, and Irene Buvat. "Partial-volume effect in PET tumor imaging". In: *Journal of nuclear medicine* 48.6 (2007), pp. 932–945.

[8] Joyita Dutta et al. "PET point spread function modeling and image deblurring using a PET/MRI joint entropy prior". In: *2015 IEEE 12th International Symposium on Biomedical Imaging (ISBI)*. IEEE. 2015, pp. 1423–1426.

[9] National Electrical Manufacturers Association (Waszyngton). *NEMA Standards Publication NU 2-2007: Performance Measurements of Positron Emission Tomographs*. National Electrical Manufacturers Association, 2007. URL: `https://books.google.pt/books?id=WhutMwEACAAJ`.

[10] G El Fakhri, R Fulton, and JE Gray. "Quality assurance for PET and PET/CT systems". In: *IAEA human health series* 1 (2009).

[11] American College of Radiology et al. *ACR-AAPM technical standard for medical physics performance monitoring of PET/CT imaging equipment*. 2018.

[12] Z Susanne et al. *NEMA image quality phantom measurements and attenuation correction in integrated PET/MR hybrid imaging. Ziegler et al EJNMMI Physics. 2015; 2: 18.*

[13] Elisabeth Pfaehler et al. "RaCaT: An open source and easy to use radiomics calculator tool". In: *PloS one* 14.2 (2019).

[14] Hidehiro Iida et al. "Three-dimensional brain phantom containing bone and grey matter structures with a realistic head contour". In: *Annals of nuclear medicine* 27.1 (2013), pp. 25–36.

[15] Kaufui V Wong and Aldo Hernandez. "A review of additive manufacturing". In: *ISRN Mechanical Engineering* 2012 (2012).

[16] Thore M Bücking et al. "From medical imaging data to 3D printed anatomical models". In: *PloS one* 12.5 (2017), e0178540.

[17] Shuai Leng et al. "Construction of realistic phantoms from patient images and a commercial three-dimensional printer". In: *Journal of Medical Imaging* 3.3 (2016), p. 033501.

[18] Terry S Yoo et al. "Engineering and algorithm design for an image processing API: a technical report on ITK-the insight toolkit". In: *Studies in health technology and informatics* (2002), pp. 586–592.

[19] G. Bradski. "The OpenCV Library". In: *Dr. Dobb's Journal of Software Tools* (2000).

[20] Olivier de Dreuille et al. "Bone equivalent liquid solution to assess accuracy of transmission measurements in SPECT and PET". In: *IEEE Transactions on Nuclear Science* 44.3 (1997), pp. 1186–1190.

[21] Will Schroeder, Lydia Ng, and Josh Cates. "The ITK software guide". In: (2003), pp. 86–88.

[22] Nicholas J Tustison et al. "N4ITK: improved N3 bias correction". In: *IEEE transactions on medical imaging* 29.6 (2010), p. 1310.

[23] Stephen M Smith. "Fast robust automated brain extraction". In: *Human brain mapping* 17.3 (2002), pp. 143–155.

[24] Rolf Adams and Leanne Bischof. "Seeded region growing". In: *IEEE Transactions on pattern analysis and machine intelligence* 16.6 (1994), pp. 641–647.

[25] R Kyle Justice and Ernest M Stokely. "3-D segmentation of MR brain images using seeded region growing". In: *Proceedings of 18th Annual International Conference of The IEEE Engineering in Medicine and Biology Society*. Vol. 3. IEEE. 1996, pp. 1083–1084.

[26] Evgeni Chernyaev. *Marching cubes 33: Construction of topologically correct isosurfaces*. Tech. rep. 1995.

[27] Thomas Lewiner et al. "Efficient implementation of marching cubes' cases with topological guarantees". In: *Journal of graphics tools* 8.2 (2003), pp. 1–15.

[28] Kenneth Clark et al. "The Cancer Imaging Archive (TCIA): maintaining and operating a public information repository". In: *Journal of digital imaging* 26.6 (2013), pp. 1045–1057.

[29] JH Hubbell and SM Seltzer. "NIST standard reference database 126". In: *Gaithersburg, MD: National Institute of Standards and Technology* (1996).

[30] Hanif Gabrani-Juma et al. "Validation of a multimodality flow phantom and its application for assessment of dynamic SPECT and PET technologies". In: *IEEE transactions on medical imaging* 36.1 (2016), pp. 132–141.